A STUDY OF INVERTER-BASED RESOURCES ON POWER GRID OPERATION UNDER UNCERTAIN OPERATING CONDITIONS

A Dissertation
Submitted to the Graduate Faculty
of the
North Dakota State University
of Agriculture and Applied Science

By

Manisha Maharjan

In Partial Fulfillment of the Requirements
for the Degree of
DOCTOR OF PHILOSOPHY

Major Department:
Electrical and Computer Engineering

January 2022

Fargo, North Dakota

NORTH DAKOTA STATE UNIVERSITY

Graduate School

Title

A STUDY OF INVERTER-BASED RESOURCES ON POWER GRID OPERATION UNDER UNCERTAIN OPERATING CONDITIONS

By

Manisha Maharjan

The supervisory committee certifies that this dissertation complies with North Dakota State University's regulations and meets the accepted standards for the degree of

DOCTOR OF PHILOSOPHY

SUPERVISORY COMMITTEE:

Dr. Di Wu
Chair

Dr. Rajesh Kavasseri

Dr. Jacob Glower

Dr. Ying Huang

Approved:

February 7, 2022
Date

Dr. Benjamin D. Braaten
Department Chair

ABSTRACT

The electric power grid is undergoing a rapid change predominantly driven by high penetration levels of renewable energy resources (RERs) such as wind and solar. These resources are interfaced with the power grid through power electronic inverters that use control algorithms to define their performance characteristics. As a group, these types of resources are commonly referred to as inverter-based RERs (IB-RERs). While IB-RERs use power electronic controls to change active and reactive power injection, the fast inverter controls, separating the power source from the grid, have changed grid dynamics and posed new challenges to maintaining reliable and safe grid operation. Moreover, the variable nature of IB-RERs generation under uncertain weather conditions further challenge the grid operation under uncertain operating conditions resulting from imbalance in electricity generation and demand. To effectively manage IB-RERs for providing reliable grid services, this dissertation studies the impact of IB-RERs on grid operation at the transmission- and distribution- levels while considering uncertain operating conditions. More specifically, probabilistic collocation method is introduced to quantify the uncertainty of renewable generation and load demands on the distribution system operation. Also, the probabilistic collocation method is integrated with grid assessment to assess the grid stiffness under uncertain operating conditions. In addition, the impact of transmission-level disturbances on solar generator operation in distribution systems is investigated by a real-time electromagnetic simulator. The proposed method and analysis results are useful for guiding grid planning and operation to address the emerging issues of integrating the high penetration of IB-RERs into the power grid for reliable grid services.

ACKNOWLEDGEMENTS

First, I would like to thank Dr. Rajesh Kavasseri for supervising my research for first two years of my PhD and most importantly encouraging me not to quit in the lowest period of my life. I am grateful to my advisor, Dr. Di Wu, for his valuable guidance and research directions which developed my research skills. Your consistent feedback and encouragement pushed me to work harder and sharpen my skills to be a better researcher.

I would also like to show gratitude to my supervising committee memebers, including Dr. Jacob Glower and Dr. Ying Huang for their valuable comments and suggestions to improve this work. I would like to acknowledge my mentors and colleagues from internships at Pacific Northwest National Lab (PNNL) and Idaho National Lab (INL) for their constructive guidelines and advices. Particularly, I would like to thank my mentors Dr. Bishnu Bhattarai and Mr. Timothy McJunkin for their patient support and the opportunities that helped me extend my research areas.

I would also like to acknowledge my colleague Almir Ekic for acquainting me with the Real-Time Digital Simulator (RTDS) and collaborating with me in different research projects. I am also grateful to everyone from the Department of Electrical Engineering at NDSU, for being kind and supporting me to successfully complete this dissertation.

In addition, I would like to thank my family and friends for their continuous encouragement and belief on me. I would not have been able to overcome the setback I faced without you all. Finally, I am grateful to all the health care workers and first responders that helped me recover from my car accident and NDSU Counseling Center for helping with my mental well-being.

DEDICATION

This dissertation is dedicated to my friend and husband Dr. Abhishek Banerjee who has persistently encouraged me in this journey.

TABLE OF CONTENTS

LIST OF TABLES

LIST OF FIGURES

1. INTRODUCTION

1.1. Background

Renewable energy resources (RERs), such as wind, solar, tidal energy paired with energy storage devices like batteries, ultra capacitors, flywheels etc. are being increasingly integrated in the modern power grid to decrease the overall global carbon footprint. In 2020, RERs generated 834 billion kWh of electricity, or about 21% of all the electricity generated in the United States [1]. The electricity generation from RERs surpassed the generation from nuclear and coal for the first time on record. Fig. 1.1 shows the annual U.S. electricity generation from utility-scale and small-scale for all the sectors including electric power, industrial, commercial and residential. The two main reasons for this surge are decreasing the use of coal for electricity generation and steady growth of RERs like solar and wind in electricity generation. Fig. 1.2 shows that among the various sources of renewable energy capacity, solar and wind capacity had a linear growth since the start of the decade [2].

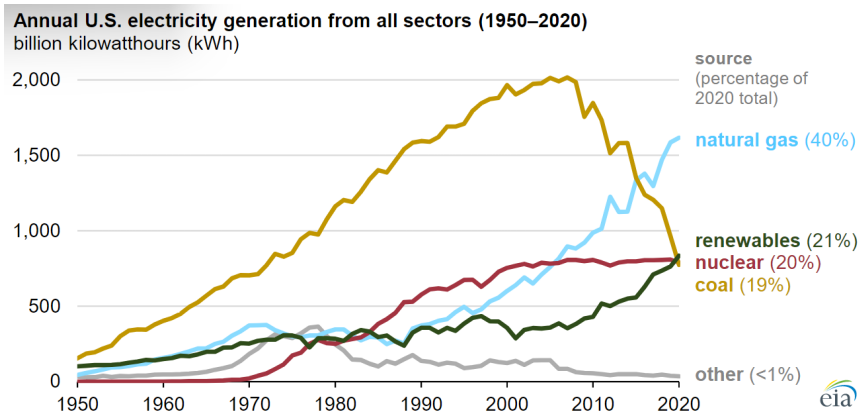

Figure 1.1. Annual U.S. electricity generation from all sectors (electric power, industrial, commercial, and residential) and includes both utility -scale and small-scale [1].

The integration of RERs deals with incorporating RERs like solar and wind, distributed generation, energy storage, and providing demand response into the transmission and distribution side of the bulk power system. It not only focuses on the operational challenges, but also deals with the economical aspects of these resources into grid planning and operation. These RERs are

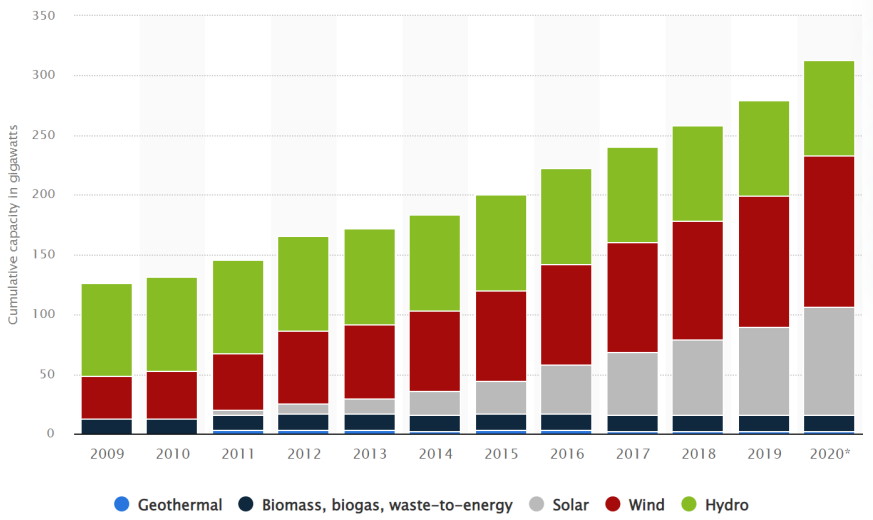

Figure 1.2. Cumulative capacity of renwable energy in the U.S. from 2009 to2020 by technology. [2].

usually connected to the grid through power electronic devices and thus are collectively referred to as Inverter Based RERS (IB-RERs). IB-RERs possess their own set of controls and operations based on power electronics devices which are much more faster that the traditional synchronous generators in the grid. IB-RERs increase the controllability, reliability and flexibility of the power grid, alongside it brings about major challenges due to its complex control, intermittent nature and concerns for protection and security. The faster timescales associated with the IB-RERs provide faster response times but due to their power electronic interface, they lack the inertial response from heavy fast spinning synchronous machines, which has been the foundation for maintaining stability and counter-acting disturbances by maintaining grid stability.

Power system planners and operators are increasingly affected by complex varieties of uncertainties pertaining on the modern grid, e.g. the volatility in generation, consumption, storage, inaccurate forecasts of weather and load, measurement errors, communication delays, instrument failure, etc. It is crucial to identify and quantify these uncertainties to realize a futuristic 100% IB-RER dominated grid, or in other words a net zero carbon grid. Considering the futuristic power grid with intermittent generation from IB-RERs, the key questions that needs to be answered are:

- Are the prevalent tools for modeling, analysis and control adequate enough for the highly unforeseeable nature of IB-RERs?
- What are the technical and economic issues that arises during high penetration of IB-RERs?

- Are the protection systems installed at present capable of protecting the power systems with a high penetration of IB-RERs?
- How can we ensure continuity and security of power supply along with voltage and frequency support to the grid from the intermittent IB-RERs?

One of the key research challenges for system analysis of the future grid is modeling uncertainties for steady-state and dynamic studies of large interconnected systems with heterogeneous generation, large number of IB-RERs in both distribution and bulk power system, centralized and distributed storage technologies, and stochastic demand with energy-efficient and electronic-interfaced loads, electric vehicles, etc [3]. To address these challenges, probabilistic approach to model uncertainties is adopted in this work to facilitate a much better understanding and more accurate prediction of the system static and dynamic behaviour. Another important area of research is the selection of appropriate method to model relevant uncertainty for proper representation in power system modeling and studies [3]. Through this dissertation work of modeling the uncertainties, an accurate prediction of the system static and dynamic behavior is achieved with considerably lower computational burden, temporally and spatially. The proposed modeling technique measures the impact of the uncertain input parameters on the system output response characteristics. The findings and outcomes of the works will help in the management of economic cost and reliability risks (grid planners, utilities, ISOs, RTOs).

Conventionally, *deterministic methods* are used to assess the performance of a system based on a specific scenario, which neglects the uncertainties in power system operation, models, and variables largely [3]. Limited number of scenarios are considered for the studies for example, the normal operation, worst-case condition, etc. Inaccurate selection of the parameters and operating conditions might lead to the problem considered being either underestimated or overestimated. The stochasticity of generation and/or load profile are expressed and modeled in the form of discrete values (e.g. high, medium and low levels). This approach does not characterize the system behavior to the full extentand does not fulfill the needs of changing landscape of the modern grid.

Conversely, *probabilistic methods* are particularly suited for analysis of system with randomness and uncertainty, which are key characteristics of future power systems. Probabilistic methods are those in which probability distribution function of the input parameters is known and based

on them the outputs can be predicted stochastically considering the process as a 'black-box' entity. This method considers the probability distribution for one, some or all the uncertain parameters, and can therefore better reflect the actual system behaviour. It aids in determining how sensitive the output is to variation of the input parameters. The parameters involved are presented in variety of scenarios considering hourly, daily, seasonal, and annual patterns, which provides more accurate estimate of true system conditions. Fig. 1.3 a visual description of the uncertainaty analysis framework. The model inputs defined are characterized by their uncertainty characteristics. The model inputs are then fed through the model (e.g. monte carlo simulation, polynomial choas methods, probabilstic colloation method, etc) and the resulting output is estimated with uncertainty analysis, e.g. by calculating the statistics like mean, variance, confidenece intervals, etc or by building histograms, probability distriubtion of the output variables.

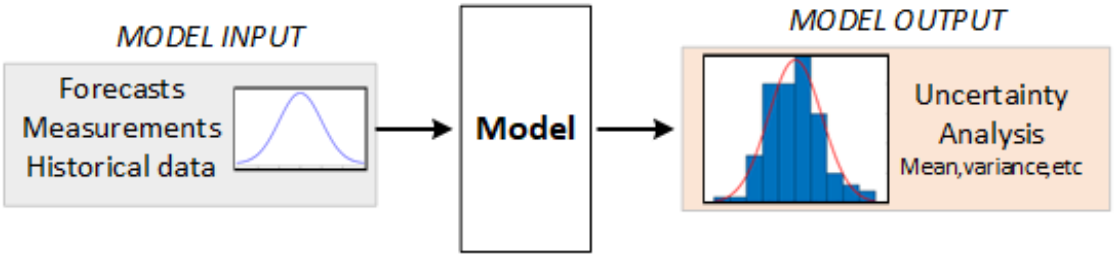

Figure 1.3. High level visualization of probabilistic approach framework.

IB-RERs are connected in both small-scale and large-scale in the power grids. The small renewables upto 5 MW are connected to the distribution grid where load is served. The distributed generation are either residential (generated behind the meter) or community-scale generation (connected to the grid via distriubtion lines). The utility-scale generation is usually greater than 20 MW, connected to the grid through transmission lines. Both types of integration of IB-RERs have operational and economic advantages to the customers and the utility operators. The distributed generation integration can significantly reduce energy losses and avoid investments on transmission and distribution infrastructure. The utility-scale generation have a larger economic benefit and its centralized nature makes it easier for grid operators to control and supervise the generation and transmission. Regardless of where IB-RERs are located in the grid, the intermittent nature of IB-RERs create challenges in the operation of the grid due to stochasticity in generation and

meeting the load requirements. As the generation is highly unpredictable, the operators need to quickly respond and control to accomodate the changing generation patterns. To provide proper representation of variability in generation in any part of the grid, this dissertation uses probabilistic approach to model uncertainty in power system studies.

1.2. Motivation

The motive of this work is to encourage power system planners and operators to incorporate the uncertainty into their system studies. This work presents a probabilistic method-based uncertainty characterization in power distribution systems considering three uncertain parameters, wind, solar and load changes simultaneously. For the utility-scale generation, this work focuses on quantifying the grid-strength of the grid connected with the intermittent IB-RERs using probabilistic method. Further, this dissertation also studies the impacts of the transmision-level disturbances on IB-RERs during fault conditions, emphasizing the need of better modeling in power system studies. The following sections discusses about various challenges addressed and contribution of this dissertation on those issues.

Increased penetration of IB-RERs and electronic loads pose operational challenges for traditional distribution systems. This intermittent nature of the IB-RERs could produce significant impact on various entities in the network like power flows, voltage profiles and losses. Modeling uncertainties plays a vital role to provide insights for decision-making to maintain stable operation of the distriubtion network. To model the uncertain parameters and investigate its impacts on the distribution network, Chapter 2 demonstrates probabilistic approach of modeling uncertainties in generation and demand, using probabilistic collocation method (PCM). PCM is used to approximate the output response in terms the uncertain input parameters by identifying a good set of simulations for correctly and robustly determining the relationship [4].

Additionally, the integration of electronic based IB-RERs such as wind, solar and storage units equipped with complex fast-acting control systems to the weaker portion of the grid has been challenging for grid planners and operators. If the grid is weak, voltage reference is less stable in a grid-following inverter based generation, which in turn affects the controls and dynamics that disrupts the overall system behavior. The integration of IB-RERs into a weak grid requires grid strength assessment in order to evaluate the possible instability and reliability risks. However, the impact of intermittent nature of these IB-RERs on grid strength has not been explored yet.

In order to account for the uncertaintites, a probabilistic approach for grid strength assessment is proposed under uncertain operating conditions by integrating PCM with grid strength metrics. The assessment provides statistical information which will aid in visualization of worst-case scenarios for the grid strength and formulates the range of grid strength metric that is achieved with minimum and maximum power injected by the integration of IB-RERs.

Along with the increased penetration of IB-RERs in power grid, IB-RERs like solar PV system experience various dynamics due to trnsmission grid disturbances [5] .Recently, the North American Electric Reliability Corporation (NERC) has reported a series of similar events of the unintended loss of solar generation in Southern California over a large geographic area following the transmission-level disturbances [6, 7, 8, 9]. These events highlight the importance of understanding the characteristics of the transmission-level disturbances propagating into the distribution systems and their impacts on the operation of IB-RERs. Therefore, to generate realistic transmission-level disturbances and investigate their impacts on the solar PV operation under different fault types and locations, solar penetration levels, and loading levels, a realistic testebed is developed in a real-time digital simulator. Such impact studies will help the operators and manufacturers to gather information for stability studies in power grid with higher penetration of IB-RERs and understand the sensitivities of IB-RERs' peformance especially during abnormal conditions.

1.3. Contributions

In summary, the contributions of the dissertation can be listed as follows.

1. To encourage inclusion of stocahsticity in power system modeling in distriubtion as well as transmission network, and define/predict operational probabilstic boundaries subjected to uncertainties, PCM is proposed to model the relation of renewable power uncertainties with various network parameters important for power system planning and operation with modeling accuracy and reduced computational burden.

2. Grid strength assessment with high penetration of RERs helps to identify the potential weak grid issues. However, the grid assessmnet techniques in the literature do not consider the intermittency of IB-RERs and lacks probabilistic representation of the grid strength assessment to consider all the possible scenarios for preparedness against systam instability. This work for the first time provides probalistic model to predict the grid strength metrics and allows

the planners and operators to analyze the grid strength under uncertain operating conditions. Furthermore, to improve the accuracy of the PCM method, K-means clustering technique is utilized to select the collocation points from historical data of the renewable genration for better representation of the data. This helps in selection of the representative simulation samples in uncertainty anlaysis of system with high number of IB-RERs efficiently.

3. Generic dynamic stability models for fault analysis of the bulk power system do not accurately reflect all aspects of the behavior of IB-RERs. Moreover, most of the research is directed towards the impacts of IB-RERs on the operation of bulk power system. To ensure that models sufficiently reflect the behavior of IB-RERs installed, a realistic testbed is utilized to investigate the transmission-level disturbances on solar PV operation under different operating conditions.

1.4. Overview of Dissertation

This dissertation consists of the materials in the following chapters that has been published in peer-reviewed conferences and journals. This dissertation is organized as follows: Chapter 2 presents the impelementation of probabilstic method for uncertainty analysis in a distribution system by modeling solar and wind power generation and load uncertainty simulatanoeusly; Chapter 3 involves proposing a probabilistic assesment of grid strength with IB-RER integration of utlity-scale with case studies with wind generation and solar generation; Cahpter 4 provides impact analysis of the transmission-level disturbances on the IB-RERs connected to the distribution side of the grid with the help of real-time simulation tool. Chapter 5 concludes this dissertation.

2. UNCERTAINTY ANALYSIS IN DISTRIBUTION SYSTEMS WITH RENEWABLE RESOURCES[1]

2.1. Introduction

Uncertainty modeling techniques are measures of the impact of uncertain input parameters on the system output response characteristics [11]. In terms of such analysis, the accuracy and computational times are the most influential factors as they determine the effectiveness of the approach when evaluating a real-time operating scenario. Several approaches have been proposed for modeling uncertain behavior in the bulk power system standpoint [12, 13, 14, 15, 16]. Probabilistic methods are those in which the probability distribution function (pdf) of the input parameters is known and based on them the outputs can be predicted stochastically considering the process as a 'black box' entity. One approach that has recently received popularity is the Probabilistic Collocation Method (PCM), which is an effective tool designed to enable uncertainty analysis of computationally expensive models at a very low computational cost [4]. It also provides a scalable computational framework for problems with multiple sources of parallel uncertainty, which requires no particular effort to segment the problem into a very large number of parallel tasks, like in case of Monte Carlo (MC) method, nor any essential dependency between those parallel tasks.

Multiple uncertain parameters are also considered in PCM for many research studies like in evaluating air traffic system performance [17] and in power system stability analysis [18, 16]. Load demand, wind, and solar PV are the most widely used system uncertainties, which have been predominately modelled by using Normal, Weibull and beta distributions, respectively [19, 20]. This work introduces PCM based uncertainty characterization in power distribution systems considering three uncertain parameters, wind, solar and load changes simultaneously.

[1]This chapter is based on the work published as "Uncertainty Analysis in Distribution Networks Integrated with Renewables by Probabilistic Collocation Method," *2020 52nd North American Power Symposium (NAPS)*, Tempe, AZ, USA, (doi: 10.1109/NAPS50074.2021.9449669) [10]. The authors of the paper are M. Maharjan, A. Banaerjee and R. G. Kavasseri. M. Maharjan was the first author and responsible for writing the manuscript and applying simulation tests. Dr. R. G. Kavasseri and Dr. A. Banerjee served as the proofreader and gave recommendations and guidance on drafting the paper.

2.2. Principle of Probabilistic Collocation Method (PCM)

PCM is an approach using Gaussian quadrature to map the relationship between the uncertain input parameters and the output [12]. It streamlines the relationship between the uncertain parameters and the desired output by identifying a good set of simulations for correctly and robustly determining the mapping. The coefficients of this polynomial mapping equation are determined by methodically selecting the collocation points [4]. The basic principles of PCM are derived from the concepts of orthogonal polynomials and Gaussian quadrature integration [4].

2.2.1. Orthogonal Polynomials and Gaussian Quadrature

Two polynomial functions $g(x)$ and $h(x)$ are orthogonal only if their inner product is zero [21]. The inner product of $g(x)$ and $h(x)$ is defined as

$$\langle g(x), h(x) \rangle = \int_{\mathbf{R}} f(x)g(x)h(x)dx \tag{2.1}$$

where $f(x)$ is any non-negative weighting function defined in a space A, and it can be represented with the probability density function (pdf) in PCM. A set of orthogonal polynomial functions $H_1(x)$, $H_1(x)$, ..., $H_n(x)$ can be defined,

$$\left\langle H_i, H_j \right\rangle = \begin{cases} 1, i = j \\ 0, i \neq j \end{cases} \tag{2.2}$$

where H_i is a polynomial of order i. For each order i, H_i has exactly i roots within the space of A. These roots are the collocation points to evaluate the coefficients of $g(x)$ used in PCM. The $(-1)^{th}$ and 0^{th} order polynomials are defined to be 0 and 1, respectively.

$$\begin{aligned} H_{-1}(x) &= 0 \\ H_0(x) &= 1 \end{aligned} \tag{2.3}$$

Gaussian quadrature integration in (2.1) approximates the numeric value for the integral by selecting appropriate x values to evaluate $g(x)$ and calculate the integral,

$$\int_{\mathbf{R}} f(x)g(x)h(x)dx \approx \sum_{i=1}^{n} f_i g(x_i) \tag{2.4}$$

where f_i is the coefficient determined by the weighting function $f(x)$, and $g(x_i)$ is computed based on x_i, which are the roots of the higher orthogonal polynomials selected based on the order of the PCM model.

2.2.2. PCM with Single Uncertainty

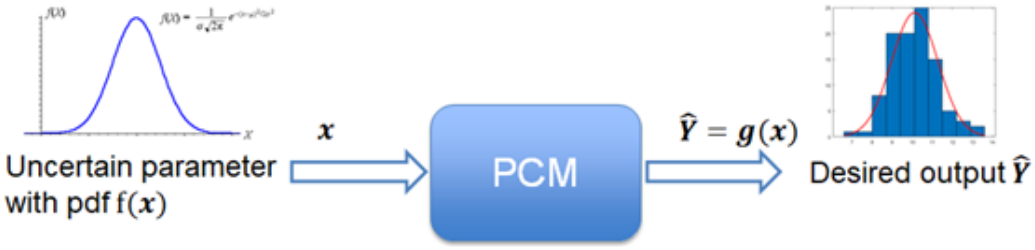

Figure 2.1. PCM with single uncertain parameter.

For a single uncertain parameter x with its pdf $f(x)$, the estimated output Y is a function of the input uncertain parameter x. The function $g(x)$ maps the relationship between x and Y. The estimated output in PCM can be written as follows.

$$\begin{aligned} \hat{Y} &= g(\hat{x}) \\ &= k_0 H_0(x) + k_1 H_1(x) + ... + k_{n-1} H_{n-1}(x) \end{aligned} \tag{2.5}$$

where k_i are constant coefficients, H_i are orthogonal polynomials of uncertain input x, and n is the order of the PCM model. The coefficients k_i are solved by replacing the estimated output and orthogonal polynomials for the collocation points.

The collocation points are selected as the roots of the next higher order orthogonal polynomial H_{n+1} of the uncertain parameter x for n^{th} order PCM model. This approach allows the collocation points to traverse the high probability regions of their distribution and to capture the

behavior of the estimated output to the fullest extent [22]. The coefficients k_i can be solved by,

$$\begin{bmatrix} k_{n-1} \\ \vdots \\ k_0 \end{bmatrix} = \begin{bmatrix} H_{n-1}(x_1) & \cdots & H_0(x_1) \\ \vdots & \ddots & \vdots \\ H_{n-1}(x_n) & \cdots & H_0(x_n) \end{bmatrix}^{-1} \begin{bmatrix} \hat{g}(x_1) \\ \vdots \\ \hat{g}(x_n) \end{bmatrix} \tag{2.6}$$

where $x_1, \ldots, x_n$ are the collocation points, $\hat{g}(x_1)$,...,$\hat{g}(x_n)$ are the responses of the output at the collocation points, and $H_0(x), \ldots, H_{n-1}(x)$ are the orthogonal polynomials calculated at the collocation points. These coefficients are replaced in (2.5) to obtain the PCM model. The statistics of the output response for a given range of the uncertain input parameter can be calculated simply using these coefficients. The expected value of output approximation $\hat{Y}$ is given by,

$$E[\hat{Y}] = E[\hat{g}(x)] = k_0, \tag{2.7}$$

and the variance of the output approximation is given by,

$$\sigma^2[\hat{Y}] = \sigma^2[\hat{g}(x)] = \sum_{i=1}^{n-1} k_i^2. \tag{2.8}$$

2.2.3. PCM with Multiple Uncertainties

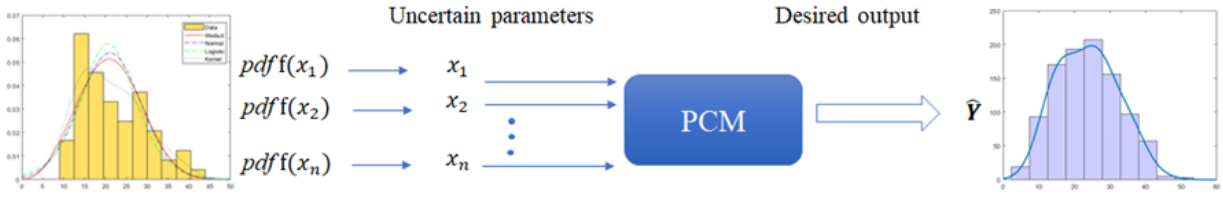

Figure 2.2. PCM with multiple uncertain parameters.

When multiple uncertain parameters $x_1, x_2, \ldots, x_n$ with independent pdfs $f(x_1)$, $f(x_2)$,..., $f(x_n)$ are considered in a system, the approximation for the output can be obtained by,

$$\hat{Y} = k_0 + \sum_{i=1}^{n} [k_{i1} H_{i1}(x_i) + ... + k_{im} H_{im}(x_i)] + \sum_{i=1}^{n} \sum_{\substack{j=1 \\ j \neq i}}^{n} [k_l H_{i1}(x_i) H_{j1}(x_j)] \tag{2.9}$$

where k_0, k_{i1}, ..., k_{im} are the coefficients, and $H_{i1}(x_i)$, ..., $H_{im}(x_i)$ are orthogonal polynomials for uncertain parameter x_i [22]. The model coefficients can be determined by using the collocation points similar to that of single uncertain parameter. However , the number of collocation points for single uncertain parameter is $(m+1)$ for m^{th} order PCM model, whereas for n uncertain parameters is given by [12],

$$1 + m \times n + \binom{n}{2} \tag{2.10}$$

For PCM modeling with multiple uncertain parameters, the number of simulation samples required for determining the coefficients increases dramatically. It is evident that as the number of input parameters and the order of orthogonal polynomials grow, the size and complexity of the approximation polynomial functions increases. Therefore, the number of input variables and the order of polynomials must be relatively small to harness the advantages of the proposed method [13].

2.3. Uncertainty Parameters

2.3.1. Wind Generation

Wind speed largely determines the quality and quantity of wind energy produced. The fluctuation of wind speed, i.e w, can be modeled as Weibull distribution [20, 23], as shown in (2.11).

$$pdf(w) = \left(\frac{k}{c}\right)\left(\frac{w}{c}\right)^{k-1} e^{\left[-\left(\frac{w}{c}\right)^{k}\right]} \tag{2.11}$$

where k is the shape factor and c is the scale factor of the weibull pdf of wind speed. The wind power generation is defined using (2.12),

$$P_{wind}(w) = \begin{cases} 0, & \text{if } w \leq w_c^{in} \\ P_r \frac{w - w_c^{in}}{w_c^{out} - w_c^{in}}, & \text{if } w_c^{in} < w \leq w_c^{out} \\ P_r, & \text{otherwise} \end{cases} \tag{2.12}$$

where w_c^{in} and w_c^{out} are the cut-in, rated and cut-out wind speed, P_r is the rated power of wind generator, and $P(w)$ is the generated power by wind turbine. The Weibull distribution based mapping, as shown in Fig.2.3, depicts the stochastic nature of wind speed with respect to wind generation based on different values for the shape factor and scale factor of the pdf.

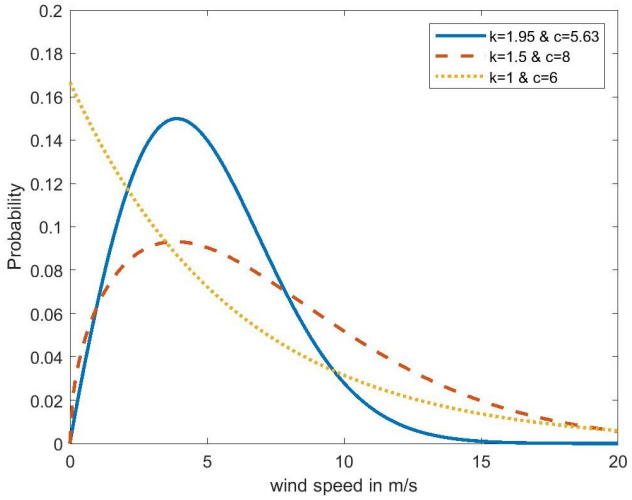

Figure 2.3. Wind speed represented by Weibull distribution.

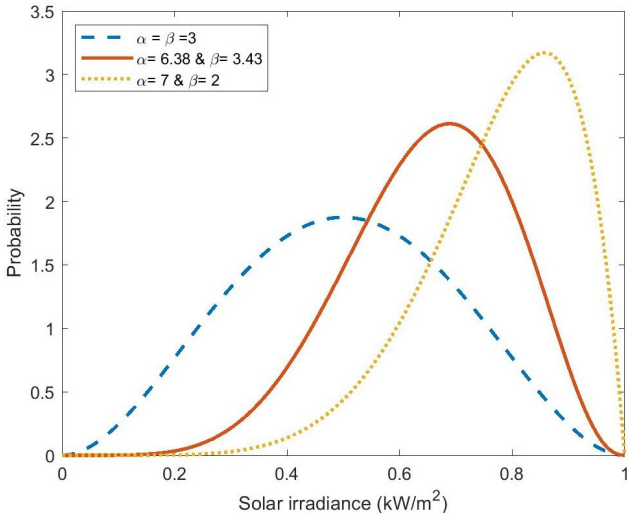

Figure 2.4. Solar irradiance represented by Beta distribution.

2.3.2. Solar Generation

The variation of irradiance data is modeled as beta distribution [24]. Equation (2.13) represents the pdf for solar irradiance.

$$pdf(s) = \begin{cases} \frac{\Gamma(\alpha+\beta}{\Gamma(\alpha)\Gamma(\beta)} \times s^{(\alpha-1)} \times \\ (1-s)^{(\beta-1)}, & \text{for } 0 \leq s \leq 1, \alpha \geq 0, \beta \geq 0 \\ 0, & \text{otherwise} \end{cases} \tag{2.13}$$

where s is solar irradiance in kW/m^2. α and β are parameters of the beta pdf. The power generated from a PV module depends on solar irradiance, ambient temperature and the module characteristics [16]. The equations in (3.20) are used to find the power generated by the PV module.

$$\begin{aligned} P_{PV}(s) &= N \times FF \times V(s) \times I(s) \\ FF &= \frac{V_{MPP} \times I_{MPP}}{V_{oc} \times I_{sc}} \\ V(s) &= V_{oc} - K_v \times T_c \\ I(s) &= s_a \times [I_{sc} + K_i(T_c - 25)] \\ T_c &= T_A + s_a \times \frac{N_{OT} - 20}{0.8} \end{aligned} \tag{2.14}$$

where T_c is the cell temperature in $°C$, T_A is the ambient temperature in $°C$, K_v, K_i are voltage and current temperature coefficient $[V/°C,\ A/°C]$, respectively, N_{OT} is the nominal operating temperature of PV cell in $°C$, FF is the fill factor, I_{sc} is the short circuit current, V_{oc} is the open circuit voltage, I_{MPP} and V_{MPP} are the current/voltage at maximum power point, and s_a is the average solar irradiance. Fig. 2.4 depicts the beta probability distribution for variation of solar irradiance with different values of α and β.

2.3.3. Loading

The active power component of the load is modeled as by normal pdf as shown in (2.15),

$$pdf(P_L) = \frac{1}{\sqrt{(2\pi\sigma)}} e^{(-\frac{(P_L - \mu)^2}{2\sigma^2})} \tag{2.15}$$

where P_L is the active power demand, and μ and σ are the mean and standard deviation of the demand respectively.

2.4. Case Studies

The IEEE 13 bus test system is modified to include the uncertain parameters and demonstrated the proposed application of PCM. There are total eight unbalanced spot loads and one distributed load in the highly loaded 4.16 kV feeder. The details of the system data can be found in [25]. The feeder is built in MATLAB/Simulink with the help of library models [26]. Three different cases with increasing number of uncertain parameters is studied and the line flows near the uncertain generation and/or consumption, and the total losses of the system are observed using

both MC simulation with 2000 iterations as well as PCM modeling technique. The simulation was carried out using High Performance Computing (HPC) in the thunder cluster of advanced research computing resources at North Dakota State University (NDSU).

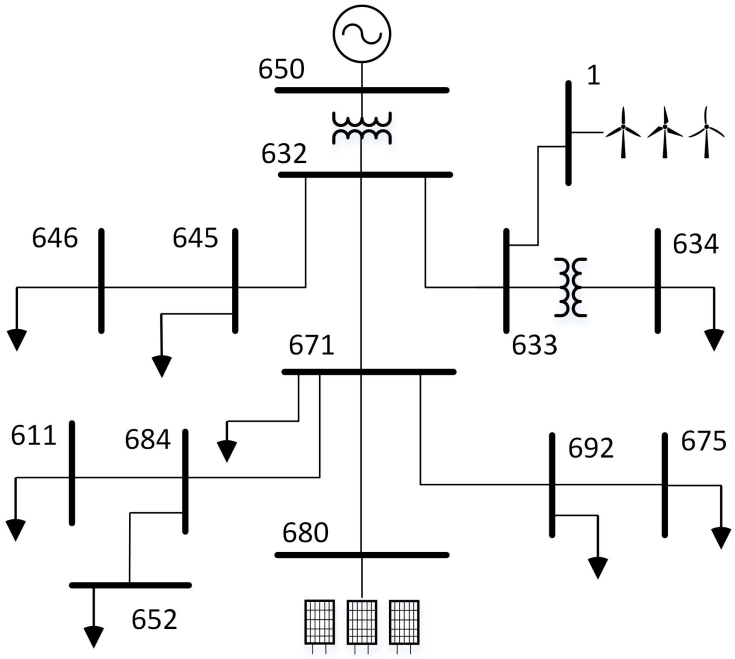

Figure 2.5. IEEE 13 bus system with wind and solar generation.

2.4.1. Uncertainty in Wind Speed

The wind speed of the wind generating farms located at bus #1 is taken as the uncertain parameter and active power line flow from bus #1 to bus #633, and the total active power loss are examined as the desired output independently. Here, for modeling the uncertainty of wind turbine, random wind speed samples are generated with the Weibull distribution, then corresponding wind power is determined using the speed power curve of the wind turbine as shown in (2.12). The shape and scale parameters of the wind speed are considered as k=5.6340 and c=1.9526. The nominal wind speed is 12.5 m/s, and the minimum and maximum operating wind speed are 3 m/s and 15 m/s respectively for the 500 kW rated power of the wind turbines.

Based on the Gram-Schmidt process [21], we can derive the first few orthogonal polynomials as,

$$\begin{aligned} H_1(w) &= w - 5 \\ H_2(w) &= w^2 - 11.7719w + 26.7273 \\ H_3(w) &= w^3 - 20.3050w^2 + 110.6824w - 154.2638 \end{aligned} \tag{2.16}$$

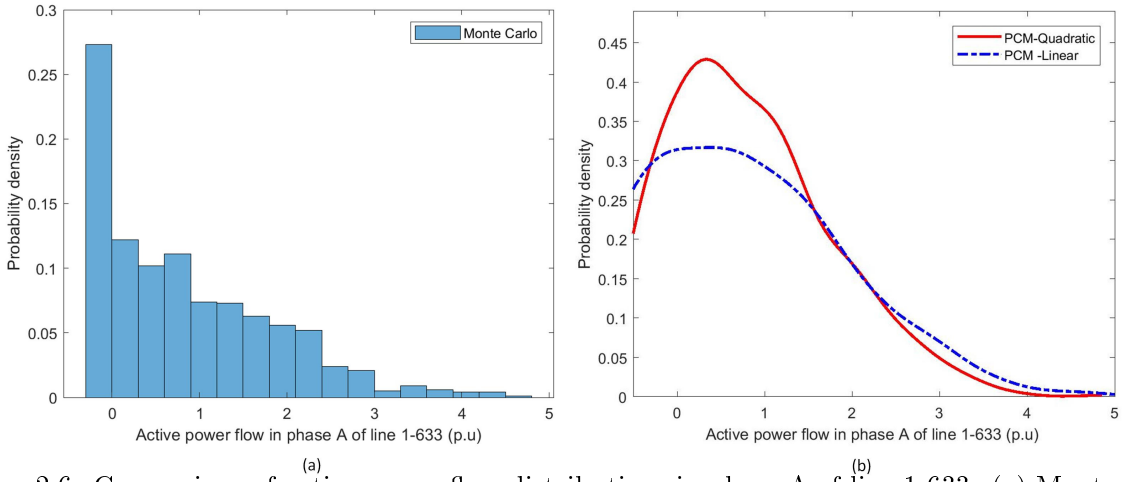

Figure 2.6. Comparison of active power flow distributions in phase A of line 1-633: (a) Monte Carlo (b) Probabilistic Collocation Method (PCM).

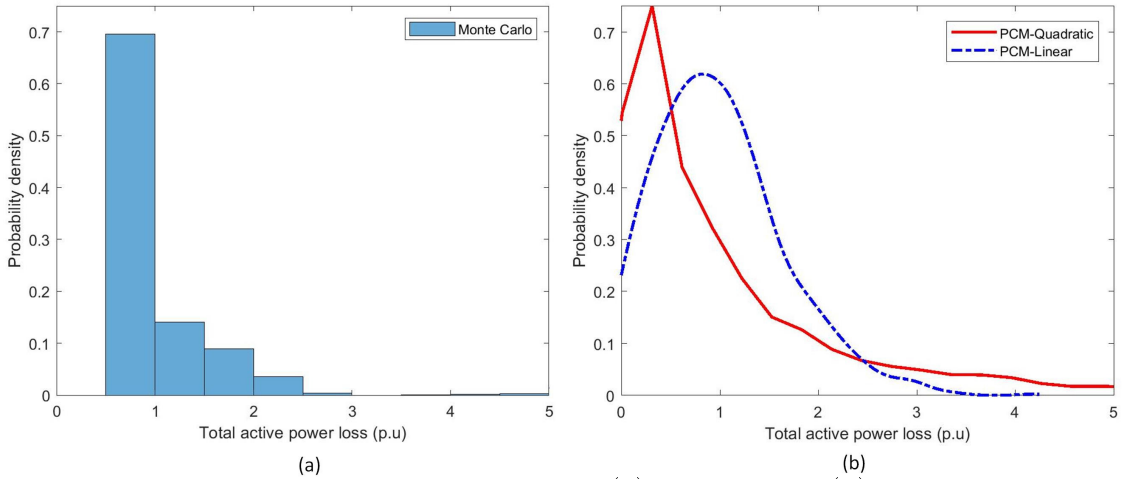

Figure 2.7. Comparison of total active power loss: (a) Monte Carlo (b) Probabilistic Collocation Method (PCM).

The roots of these orthogonal polynomials are used to evaluate the coefficients of the PCM approximation. The response from the obtained collocation points and the orthogonal polynomials are utilized to form the linear and quadratic equations. The mean and variance of the desired outputs from the PCM mapping and Monte Carlo simulation with 2000 sample points are presented in Table 2.1. The mean of both linear and quadratic PCM approximation are almost close to the mean obtained from MC simulation. Also, the quadratic approximation gives better results than the linear approximation. However, the variances can be seen are varying between the MC simulations and PCM. From the Fig. 2.6 and Fig. 2.7, it can be seen that PCM can predict the probability of the output significantly, since the mapping was done with regards to the high probability region.

Table 2.1. Mean and variance for uncertainty in wind speed

	Monte Carlo		**PCM -Linear**		**PCM- Quadratic**	
Flow	μ	σ^2	μ	σ^2	μ	σ^2
1-633[A]	0.8491	0.9522	0.7410	0.1838	0.8341	0.1097
1-633[B]	0.8121	0.8179	0.7134	0.1691	0.8860	0.1489
1-633[C]	0.8885	1.0630	0.7507	0.1840	0.942	0.1695
Loss	1.1216	2.1905	1.0210	0.0605	1.4431	0.4585

2.4.2. Uncertainty in Wind Speed and Loading

The wind speed of the wind generation located at bus #1 and the load situated at bus #611 are taken as the two input uncertain parameters. The load at bus #611 is a single phase load at phase C of the unbalanced system. The load uncertainty follows normal distribution with μ_X=2 and σ_X=1. The normally distributed parameter X can be represented as [13],

$$X = \mu_X + \sigma_X(H_1(\zeta)) \tag{2.17}$$

where μ_X and σ_X are the mean and standard deviation of the uncertain parameter X, and $H_1(\zeta)$ represents the first order orthogonal polynomial of the standard normal distribution ζ. The orthog-

onal polynomials of ζ are given by the Hermite polynomials.

$$\begin{aligned} H_1(\zeta) &= \zeta \\ H_2(\zeta) &= \zeta^2 - 1 \\ H_3(\zeta) &= \zeta^3 - 3\zeta \end{aligned} \tag{2.18}$$

Table 2.2. Mean and variance for uncertainty in wind speed and loading

	Monte Carlo		**PCM -Linear**		**PCM- Quadratic**	
Flow	μ	σ^2	μ	σ^2	μ	σ^2
684-611	3.3181	2.4099	3.2830	2.6354	3.2830	2.6343
1-633[C]	0.8951	1.2101	0.7507	0.1840	0.9108	0.1459
Loss	1.2076	2.0533	1.1054	0.0677	1.7899	0.8792

Now using (2.10), we can find the number of collocation points required to model the PCM model. The roots of the orthogonal polynomials of both the uncertain parameters are used to choose collocation points. The collocation points pairs are selected in such a way that at least one highest probability value of uncertain parameters is included. The statistics of the results for this case is shown in Table 2.2. The variances for line flow $684 - 611$ are significantly accurate as the data is consistently unidirectional unlike the other two variables.

2.4.3. Uncertainty in Wind Speed, Loading and Solar Irradiance

Three uncertain parameters - wind generation, loading and solar generation, are taken into consideration. The solar generation is located at bus #680 with rated power of 500kW. The shape parameters of solar irradiance are considered as $\alpha = 6.38$ and $\beta = 3.43$. For the characteristics of PV module, the values taken are $I_{sc} = 5.32$A, $V_{oc} = 21.98$V, $I_{MPP} = 4.76$A, and $V_{MPP} = 17.32$V. The temperature coeffcients are $k_v = 14.40\ mV/^\circ C$ and $k_i = 1.22\ mA/^\circ C$. The nominal operating temperature of PV cell $N_{OT} = 43^\circ C$. The orthogonal polynomials generated for solar irradiance s

using [27] are as follows:

$$\begin{aligned} H_1(s) &= s - 0.3751 \\ H_2(s) &= s^2 - 0.7863s + 0.1359 \\ H_3(s) &= s^3 - 1.2201s^2 + 0.4472s - 0.0478 \end{aligned} \tag{2.19}$$

These orthogonal polynomials along with the ones for wind speed and loading are used to model PCM equations by simulating few collocation points. The results are summarized in Table 2.3 which shows comparable means for both variables. The variances are at ballpark, that might be due to the nature of bidirectional flows in the network, which is not completely captured by the PCM model.

Table 2.3. Mean and variance for uncertainty in three parameters

	Monte Carlo		**PCM -Linear**	
Flow	μ	σ^2	μ	σ^2
680-671[C]	0.4611	0.0357	0.3089	2.2281
Loss	1.1413	1.8331	1.0859	0.0781

Finally, Table 2.4 compares the computational time for the MC and the PCM based methods, clearly depicting the advantage of proposed PCM based uncertainty modeling approach which is able to approximate the ouptut in significantly lesser time.

Table 2.4. Computation time for Monte Carlo and PCM

Method	Monte Carlo	PCM : 2 samples	PCM : 3 samples
CPU time (s)	1310.20	8.51	12.39

2.5. Summary

Uncertainty in IB-RER like wind speed, loading and solar irradiance were introduced using Weibull, Normal and Beta distribution respectively in a distribution test bed. Probabilistic Collocation Method (PCM) was used to model these uncertain input parameters and approximate the line flows and total loss of the test system. The output from the approximation was compared with

multiple Monte Carlo simulation runs. The results depict that the model was able to achieve accurate mean and ballpark variance of the output variables. As the number of uncertain parameters increase, the PCM mapping becomes more complex due to increase in number of collocation point-pairs and model coefficients. A quick estimate can be made using PCM with significantly smaller number of model runs than Monte Carlo before leveraging time and cost for detailed computational analysis.

3. PROBABILISTIC GRID STRENGTH ASSESSMENT FOR TRANSMISSION SYSTEMS WITH HIGH PENETRATION OF RENEWABLE RESOURCES[1]

3.1. Introduction

Many inverter-based renewable energy resources (IB-RERs) are integrated onto the electric power grid in the world to reduce greenhouse gas emissions. Most renewable energy resources are interfaced with the power grid through power electronic inverters. While the IB-RERs supply clean energy to electricity customers, they are also challenging grid planning and operation. The IB-RERs provide expected real and reactive power based on the electronic controls, which separate the power source from the grid. These controls, may in turn, depend on a stable voltage reference from the grid. As the grid is weakened, the voltage reference becomes less stable, and control dynamics and tuning become increasingly influential on overall system behavior [29]. Wind and solar power are different from most thermal generators since they have variable and uncertain power output determined by local weather conditions. The weak grid issues may become prominent due to the variability and uncertainty of IB-RERs [30, 31].

Potential weak grid issues are usually analyzed and identified based on grid strength assessment. In the assessment, short-circuit ratio (SCR) is an index recommended by North American Electric Reliability Corporation (NERC) to quantify the grid strength [29, 32]. The commonly used SCR calculation method ignores the interactions among IB-RERs and thus may cause an inaccurate estimation of grid strength at points of interconnection for IB-RERs [29, 33]. To consider the effect of IB-RERs interactions on grid strength, several new methods have been developed, such as the weighted short-circuit ratio (WSCR) method developed by the Electric Reliability Council of Texas [33] and the composite short-circuit ratio (CSCR) method developed by GE Energy Con-

[1]This chapter is based on the work submitted as "Probabilistic Grid Strength Assessment of Power Systems with Uncertain Renewable Generation based on Probabilistic Collocation Method," *17th International Conference on Probabilistic Methods Applied to Power Systems (PMAPS)* [28] and journal being drafted as "Uncertainty Evaluation Method for Grid Strength Analysis Under Uncertain Renewable Generation ". The authors of the paper are M. Maharjan, A. Ekic and D. Wu. M. Maharjan was the first author and responsible for writing the manuscript, developing the methodology, and implementing the case studies for simulation results. A. Ekic assisted in verfication of the results and writing the manuscript, and Dr. D. Wu gave guidance on the methodology, provided resources and wrote the manuscript.

sulting [34]. Both the CSCR and the WSCR methods do not consider the real electrical network connections among IB-RERs, which may not reflect the actual strength of the grid at the POIs. Also, both the CSCR and WSCR methods mainly provide the aggregated strength of a power grid in the area where the IB-RERs are interconnected electrically close, but they do not calculate the strength of the grid at each individual POIs in the specific area. To overcome those shortcomings, the site-dependent short-circuit ratio (SDSCR) method is proposed in [35] by analyzing the relationship between grid strength and voltage stability. However, SDSCR does not consider the impact of the shunt capacitors at POIs on grid strength. To consider the impacts of capacitor compensation for grid strength assessment, [36] proposed a novel method for evaluating the grid strength using effective site-dependent short-circuit ratio (ESDSCR). This method considers the interactions between the IB-RERs and between the shunt capacitors at POIs of IB-RERs.

Although various methods have been proposed to improve grid strength assessment, it is still challenging to evaluate grid strength while considering the impact of uncertain renewable generation. Commonly, Monte Carlo simulation (MCS)-based methods are used to obtain the possible states of IB-RERs [37, 38, 39]. However, when integrating MCS with the SDSCR-based method, its computational cost is expensive. Moreover, the computation cost is significantly increased when considering the impact of IB-RER interaction on grid strength assessment in power systems with high penetration of IB-RERs.

To address the challenges, the paper proposes a probabilistic approach for grid strength assessment of power systems under uncertain renewable generation by integrating the probabilistic collocation method (PCM) with the SDSCR-based method and the ESDSCR-based metod. The PCM has been studied for uncertainty analysis in numerous power system studies [12, 4, 22, 13, 40]. The PCM is used to establish the probabilistic approximation function to model the impact of uncertain renewable generation. Since the PCM can obtain accurate results using a small set of simulations, this method can be potentially used to save the computational cost.

3.2. Grid Strength Assessment

Grid strength assessment can help grid engineers identify and understand "weak" grid issues for reliably planning and operating the power grid. Grid strength is a characteristic of an electrical power system that relates to the size of the change in voltage following a fault or disturbance on the power system [41]. It helps to quantify the effect of integration of IB-RERs on power grid stability

and operation. The stronger a grid is, the less risks the grid will have for weak grid issues. The strength of a power grid at a point of interconnection (POI) is commonly quantified by SCR, which is the ratio of the short circuit capacity at the POI to the rated capacity or injected power from the IB-RER [42]. That is,

$$SCR_i = \frac{|S_{ac,i}|}{P_{R,i}} = \frac{|V_{R,i}|^2}{P_{R,i}} . \frac{1}{|Z_{R,i}|} \tag{3.1}$$

where symbol |.| indicates the magnitude of a complex quantity; $S_{ac,i} = |V_{R,i}|^2/|Z_i|$ is the short-circuit capacity of the grid at POI i; $V_{R,i}$ is the voltage at POI i; Z_i is the Thevenin equivalent impedance seen at POI i; and $P_{R,i}$ is the rated capacity or injected power from the IB-RER at POI i.

The SCR defined in (3.1) does not account for the interactions among multiple IB-RERs. Especially, when IB-RERs are electrically close, the interactions have significant impacts on the strength of their POIs. To include the impact for grid strength assessment, SDSCR was proposed in [35] by analyzing the relationship between the SCR and voltage stability in a power grid with a single IB-RER and then extending this relationship to a power grid with multiple IB-RERs. The SDSCR is defined as [35],

$$SDSCR_i = \frac{|V_{R,i}|^2}{(|P_{R,i} + \sum_{j \epsilon R, j \neq i} w_{ij} P_{R,j}|)|Z_{RR,ii}|} \tag{3.2}$$

$$w_{ij} = \frac{Z_{RR,ij}}{Z_{RR,ii}} . \left(\frac{V_{R,i}}{V_{R,j}}\right)^* \tag{3.3}$$

where R is the set of all POIs connected to IB-RERs; $Z_{RR,ij}$ is the (i^{th}, j^{th}) element in submatrix of bus impedance matrix that is only related to buses connected to IB-RERs; and symbol * indicates the complex conjugate of a complex quantity.

The SDSCR defined in (4.1) takes into account the impact of the interactions among IB-RERs on the grid strength at POI i by interaction factors w_{ij}, which includes two ratios: the ratio of electrical distance $Z_{RR,ij}/Z_{RR,ii}$ and the ratio of conjugated voltages $V^*_{R,i}/V^*_{R,j}$. The SCR in (3.1) can be considered as a special case of the SDSCR when only one IB-RER is connected to the power grid. Thus, the ranges of SCR for grid strength evaluation can also be applied to SDSCR.

That is, the grid is strong at a POI if its SDSCR value is larger than 3; the grid is weak at a POI if its SDSCR value is between 2 and 3; and the grid is very weak at a bus if its SDSCR value is smaller than 2 [43]. As shown in (4.1), the SDSCR is related to renewable generation PR,i at different POIs. When the renewable generation is uncertain, the SDSCR evaluation is required for all feasible uncertain scenarios, which is computationally daunting. To address the challenge, the paper proposes a probabilistic approach by integrating the PCM with the SDSCR-based method to reduce computational cost compared with the MCS.

Morever, SCR does not include the effect of the reactive power compensation from the shunt capacitor at the buses for measuring the grid strength. To account for the impact of shunt capacitor, the grid strength is calculated using effective short circuit ratio (ESCR), which is defined as [44],

$$ESCR_i = \frac{|S_{ac,i} - jQ_{c,i}|}{P_{R,i}} \tag{3.4}$$

where $Q_{c,i} = |V_{R,i}|^2/|X_c|$ is the reactive compensation from shunt capacitor at POI i.

Eventhough ESCR defined in (3.4) considers the impact of the reactive power compensation from shunt capacitor at POI on grid strength, it fails to account for the interactions among the capacitors and the interactions among multiple IB-RERs in a power grid. Especially, when IB-RERs are electrically close, the interactions have significant impacts on the strength of their POIs. To include these impacts for grid strength assessment, the effective site-dependent SCR (ESDSCR) was proposed in [36] by establishing the relationship to express the impacts of interconnected capacitors on voltage stability in a power grid with a single IB-RER and then extending this relationship with multiple IB-RERs. The ESDSCR is defined as [36],

$$\begin{aligned} ESDSCR_i &= \frac{|S_{ac,i} - jQ_{ceq,i}|}{P_{Req,i}} \\ &= \frac{|S_{ac,i} - jQ_{c,i} - \sum_{j\epsilon R, j\neq i} \alpha_{ij} jQ_{c,j}|}{(|P_{R,i} + \sum_{j\epsilon R, j\neq i} \beta_{ij} P_{R,j}|)} \end{aligned} \tag{3.5}$$

$$\alpha_{ij} = \frac{Z_{RR,ij}}{Z_{RR,ii}} . \left(\frac{V_{R,j}}{V_{R,i}}\right) \tag{3.6}$$

$$\beta_{ij} = \frac{Z_{RR,ij}}{Z_{RR,ii}} \cdot \left(\frac{V_{R,i}}{V_{R,j}}\right)^* \tag{3.7}$$

where R is the set of all POIs connected to IB-RERs; $Z_{RR,ij}$ is the (i^{th}, j^{th}) element in submatrix of bus impedance matrix that is only related to buses connected to IB-RERs; and symbol * indicates the complex conjugate of a complex quantity.

The ESDSCR defined in (3.5) takes into account the impact of the interactions among IB-RERs and capacitors on the grid strength at POI i by interaction factors α_{ij} and β_{ij}. The ESDSCR at bus i accounts for the reactive compensation from the shunt capacitor connected at bus i ($Q_{c,i}$) and the reactive compensation from other capacitors in different locations ($Q_{c,j}$) with the interaction factor α_{ij} as defined in (3.6). Moreover, ESDSCR at bus i utilizes the real power injected by the IB-RER directly connected to bus i ($P_{R,i}$) and the real power injection from other IB-RERs at different locations in the power grid ($P_{Req,i}$), scaled by the interaction factor β_{ij} as defined in (3.7).

The ESCR in (3.4) can be considered as a special case of the ESDSCR when only one shunt element is connected to one IB-RER in the power grid in (3.4). Thus, the ranges of ESCR for grid strength evaluation is also relevant to ESDSCR. For instance, if the ESDSCR value is larger than 3 ($ESDSCR > 3$), then the power grid is strong at a POI ; if ESDSCR value is between 2 and 3 ($2 < ESDSCR < 3$), the grid is weak at a POI; and if ESDSCR value is smaller than 2 ($ESDSCR < 2$), the grid is very weak at a POI. From (3.5), it is evident that the ESDSCR is related to renewable generation $P_{R,i}$ at different POIs. ESDSCR values should not only be calculated for a deterministic scenario, but should be computed for all possible scenarios that can occur in power grid. When the renewable generation is uncertain, the ESDSCR evaluation is required for all feasible uncertain scenarios, which is computationally daunting. To address the challenge, this paper proposes a probabilistic approach by integrating the PCM with the SDSCR-based method and the ESDSCR-based method to reduce computational cost compared with the MCS.

3.3. K-means Method for Generating Collocation points

PCM method requires fewer number of simulation model runs to find the coefficients of a good approximation of the output response. This not only saves simulation time but also save computational burden with respect to MCS method. It is crucial to select these simulation points, also known as collocation points, accurately as these represent the probabilistic behavior of the

uncertain parameter [40]. Traditional PCM method selects the collocation points using the roots of the next higher order orthogonal polynomials for each uncertain parameter [4, 12].

In this dissertation, k-means clustering algorithm is compared with the traditional root methd for selection of the collocation points. K-means clustering method is a standard algorithm used for dimensionality reduction which adequately represents the data into smaller sample [45, 40]. This method splits N number of data to k clusters where each data point belongs to the cluster with the closest centroid, acting as the representative of the overall cluster. Mathematically, it minimizes the sum of the Euclidean distances between the each data point and the centroid in each cluster, which is written as,

$$\min \sum_{k=1}^{N_k} \sum_{i=1}^{n_k} ||\xi_i - c_k||^2 \tag{3.8}$$

where ξ_i is the collection of data points, c_k is the centroid of the k cluster with n_k data points, N_k is the number of clusters, and $||\xi_i - c_k||$ is the Euclidean distance (point to cluster distance) between ξ_i and c_k. Thus, N_k cluster centroid are obtained that includes significant samples of the total data, and is used to represent the collocation points for better approximation using PCM model. The algorithm of K-means clustering is applied using the following steps:

1. Define the number of the clusters N_k.
2. Choose initial data points as cluster centroids c_k.
3. Compute the point to cluster centroid distances of all the data points to each centroid.
4. Reassign the data point to different cluster with minimum point to cluster distance.
5. Calculate the average of the data points of each cluster to obtain k new centroid location.
6. Repeat steps 3)-5) unless the cluster assignments do not change.

3.4. Probabilistic Approximation Method for Grid Strength Assessment Power Grid Integrated with Wind Energy

To assess grid strength of power systems under variable renewable generation, the grid strength metric-based method is integrated with the PCM, which models the impact of uncertain renewable generation probabilistically based on their historical data and evaluates the probabilistic

results instead of deterministic values. The method is developed under two main case studies. First case study includes the grid strength metric SDSCR is approximated using PCM with wind power generation as uncertain renewable genration and in the other case study, the grid strength metric ESDSCR is approximated using PCM with solar power as uncertain renewable genration. The modeling, algorithm, and simulations studies for each case is described in details in rest of this chapter.

3.4.1. Probabilistic Model of Wind Power Generation

The actual historical data can demonstrate the uncertainty characteristic of renewable generation. For example, uncertain wind generation is related to variable wind speed. Thus, the forecasted or the historical data for wind speed can be used for probabilistically modeling the uncertain feature of wind generation. The mechanical power output P of wind turbine can be calculated using [46],

$$P = \frac{\rho}{2} \times A_r \times w^3 \times C_p(\lambda, \theta) \tag{3.9}$$

where ρ is the air density, A_r is the area swept by the rotor blades, λ is the tip seed ratio, θ is the pitch angle, and C_p is the power coefficient, which is the function of λ and θ, w is the wind speed, and its uncertainty can be represented by the Weibull distribution below [22],

$$f(w) = \left(\frac{k}{c}\right)\left(\frac{w}{c}\right)^{(k-1)} e^{[-(w/c)^k]} \tag{3.10}$$

where f is the pdf of the wind speed, k is the shape factor and c is the scale factor of the distribution of wind speed w. Fig. 3.1 shows the pdf curve of wind speed that is used in this paper.

To derive the orthogonal polynomials of wind speed for the application of the PCM, we consider the associated Laguerre polynomial which is orthogonal over [0, ∞) with respect to the weighting function $x^z e^{-x}$ with an arbitrary real z.

$$\int_0^\infty x^z e^{-x} L_i^{(z)}(x) L_j^{(z)}(x) dx = 0, \qquad i \neq j \tag{3.11}$$

The weighting function for the Weibull distribution can be rearranged to be expressed in the form of the Laguerre polynomial [22]. Thus, the orthogonal polynomials for the representative

distribution can be derived by the method described in [27]. Equation (3.11) can be rearranged by comparing it with the Weibull distribution and is written as in terms of y as a transitional variable.

$$\int_0^\infty y^{\frac{k-1}{k}} e^{-y} H_i(y) H_j(y) dy = 0, \qquad i \neq j \tag{3.12}$$

where

$$y = \left(\frac{x}{c}\right)^k \tag{3.13}$$

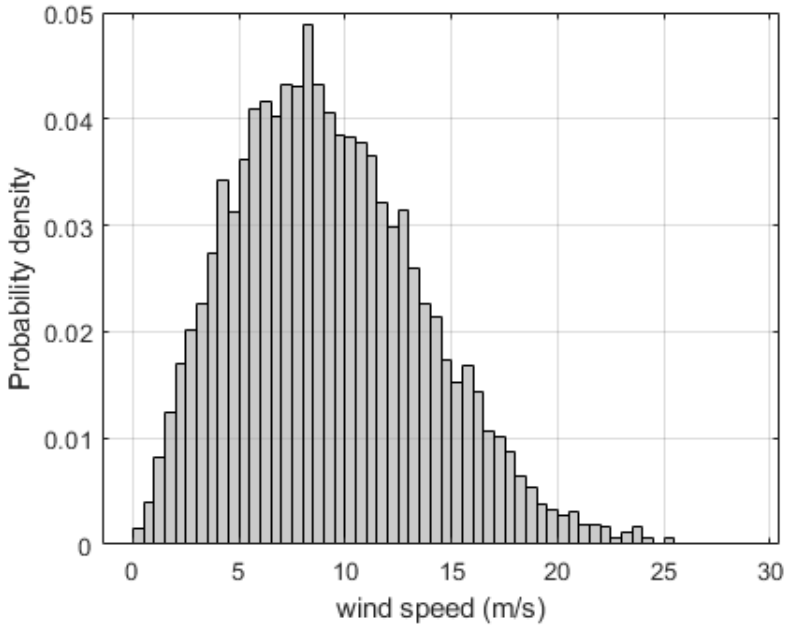

Figure 3.1. Probability density of wind speed with Weibull distribution.

Based on (3.12) and the Gram-Schmidt process [21], the orthogonal polynomials for the wind speed in wind generators can be derived such as the those listed Tabl 3.1, where $G_i(y_1)$ represents the orthogonal polynomials for wind generator 1 and $H_i(y_2)$ for wind generator 2. The roots from $G_i(y_1)$ and $H_i(y_2)$ is later converted back to relevant wind speeds. Using these wind speeds, the coefficients of the approximation model for SDSCR can be evaluated.

Table 3.1. Parameters and orthogonal polynomials for wind generators

Wind Generator 1
$G_1(y_1) = y_1 - 1.4872$
$G_2(y_1) = (y_1)^2 - 4.9743y_1 + 3.6988$
$G_3(y_1) = (y_1)^3 - 10.4615(y_1)^2 + 26.0197y_1 - 12.8986$
$G_4(y_1) = (y_1)^4 - 17.9487(y_1)^3 + 93.8856(y_1)^2 - 155.6735y_1 + 57.8786$
...
Wind Generator 2
$H_1(y_2) = y_2 - 1.5454$
$H_2(y_2) = (y_2)^2 - 5.0909y_2 + 3.9338$
$H_3(y_2) = (y_2)^3 - 10.6363(y_2)^2 + 27.0743y_2 - 13.9474$
$H_4(y_2) = (y_2)^4 - 18.1818(y_2)^3 + 96.6942(y_2)^2 - 164.0871y_2 + 63.3973$
...

3.4.2. Probabilistic Evaluation of SDSCR

By integrating the PCM with the SDSCR-based method, the main steps of the proposed approach for probabilistically assessing grid strength of power systems under uncertain renewable generation can be summarized as follows:

1. Obtain the actual historical/predicted data of uncertain input parameters such as wind speed, wind power generation, and convert into intermediate variable using (3.11)-(3.12) to obtain appropriate pdf of uncertain parameters. Evaluate orthogonal polynomial functions from the obtained pdf based on equations (2.1)-(2.3).

2. Develop the polynomial models of the output response with respect to input variables of corresponding wind speed in step 1) using (2.5) or (2.9) and unknown coefficients.

3. Compute the collocation points from the orthogonal polynomials in step 1) and run power flow calculation at these points to find the corresponding output of SDSCR defined in (4.1).

4. Use these collocation points calculated and the corresponding output of SDSCR in step 3) to obtain the unknown coefficients of the approximation model for SDSCR developed in step 2) to assess grid strength under uncertain wind generation.

3.4.3. Estimating SDSCR using PCM in IEEE 9 bus sytem

The efficacy of the proposed method for probabilistically assessing grid strength of power systems under uncertain renewable generation is demonstrated on the modified IEEE 9-bus system as shown in Fig. 3.2, where two synchronous generators at buses 1 and 2 are replaced with two doubly fed induction generators (DFIGs). The parameters of the two DFIGs are presented in Table 3.2.

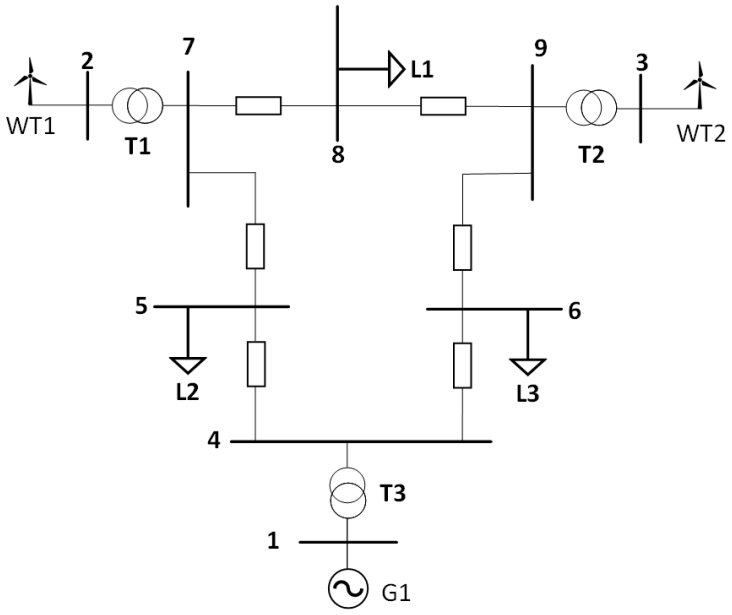

Figure 3.2. The modified IEEE 9 bus system with two DFIGs.

Table 3.2. Parameters for DFIGs

Parameters	DFIG 1	DFIG 2
Shape and scale parameters	k1 = 1.95	k1 = 2.2
	c1 = 8	c1 = 10.5
Cut-in speed (m/s)	3	3
Cut-out speed (m/s)	15	15
Rated power (MW)	100	50

The sum- squared-root error (e_{SSR}) is computed as an index for quantifying the approximation accuracy [22] .

$$e_{SSR} = \sqrt{\frac{\sum_{i=1}^{\eta} (\hat{Y}_i - Y_i)^2 f(\vartheta_i)}{\eta f(\hat{\vartheta})}} \tag{3.14}$$

where Y_i is the actual output from the simulation run, $\hat{Y}_i$ is the estimated output, η is the collocation points, $f(\vartheta_i)$ is the joint pdf and $f(\vartheta)$ is the pdf of the highest probability collocation point.

3.4.3.1. PCM Simulation in Various Orders

In the case study, the PCM simulation results of SDSCR at buses 1 and 2 with different orders (1^{st} –4^{th} order) in the approximation model are compared with MCS results. The approximation errors for each order of approximated model are calculated based on (3.23). Table III compares the errors, the mean value, the variance value, computational times, and the required simulation runs. Equations (3.15)-(3.18) shows the 1^{st} –4^{th} order PCM approximations for SDSCR at bus 2 in terms of transitional variable y shown in (3.12) and (3.13). Fig. 3 shows the pdf curves from MCS and the approximation models of four different orders for SDSCR at bus 2. Fig. 4 shows the cumulative distribution function (cdf) curves from MCS and the 3^{rd} and 4^{th} order approximation models for SDSCR at bus 2.

$$\hat{g}(y) = 0.4048y_1 + 0.1086y_2 + 2.3751 \tag{3.15}$$

$$\hat{g}(y) = -0.1243y_1^2 + 1.4432y_1 - 0.6702y_2 + 0.3126y_1y_2 + 3.2943 \tag{3.16}$$

$$\hat{g}(y) = 0.0289y_1^3 - 0.51033y_1^2 + 0.9942y_2^2 + 2.8807y_1 - 3.8206y_2 - 0.6954y_1y_2 + 4.9415 \tag{3.17}$$

$$\hat{g}(y) = 0.0134y_1^4 - 0.3405y_1^3 - 0.3534y_2^3 + 2.5740y_1^2 + 4.0564y_2^2 - 5.9685y_1 - 10.0699y_2 + 0.7323y_1y_2 + 4.9415 \tag{3.18}$$

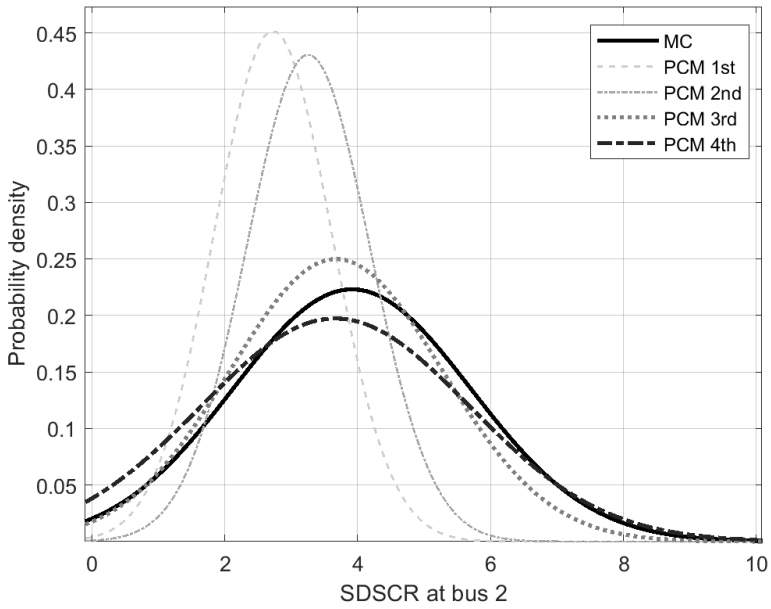

Figure 3.3. Probability distribution function (pdf) plot for SDSCR at bus 2.

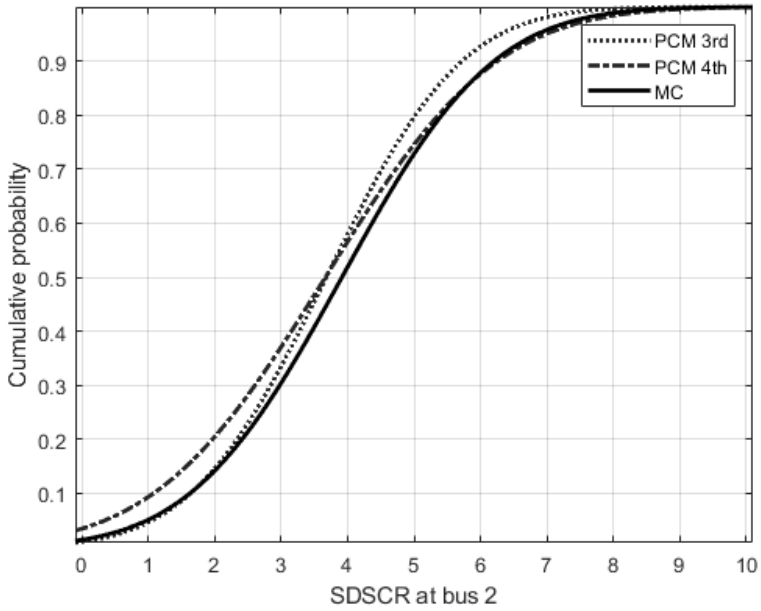

Figure 3.4. Cumulative probability function (cdf) plot for SDSCR at bus 2.

It can be observed from Fig. 3.3 and Fig. 3.4 as well as Table 3.3 that the 3^{rd} approximation model provides a better estimation of SDSCR than the 1^{st}, 2^{nd}, or 4^{th} order PCM models under uncertain wind generation. As shown in Fig. 3.3 and Fig. 3.4, the 3^{rd} and 4^{th} order PCM models provide estimated pdfs and cdfs closer to the those from MCS than the 1^{st} and 2^{nd} order models.

Moreover, Table 3.3 shows the means and variances from the 3^{rd} order PCM model (i.e., 3.67 and 2.54) and the 4^{th} order PCM model (i.e., 3.66 and 4.08) are closer to those from MCS (i.e., 3.91 and 3.19) than those of the 1^{st} and 2^{nd} order PCM models. By comparing the 3^{rd} with the 4^{th} order PCM models, the 3rd order PCM model has the mean and variance closer to those from MCS, though the 3^{rd} with the 4^{th} order PCM models have similar errors (i.e., 0.2820 and 0.2714). Moreover, the 3^{rd} PCM model takes less time and effort than the 4^{th} PCM model. Thus, the 3rd PCM approximation model provides a better estimation of SDSCR.

Table 3.3. Comparison of MCS with PCM models for SDSCR

	MCS	PCM 1^{st}	PCM 2^{nd}	PCM 3^{rd}	PCM 4^{th}
mean	3.91	2.72	3.25	3.67	3.66
variance	3.19	0.78	0.85	2.54	4.08
e_{SSR}	-	0.6280	0.4934	0.2820	0.2714
runs	5000	3	8	15	24
time(s)	102.71	4.32	4.91	5.11	5.91

Furthermore, it can be seen from Fig. 3.3 and Fig. 3.4 as well as Table 3.3 that the proposed method for probabilistic grid strength assessment can save a substantial amount of computational time compared with traditional MCS. As shown in Table 3.3 and Fig. 3.3 and Fig. 3.4, the MCS requires 5000 simulations to obtain the pdf of SDSCR for given range of uncertain parameters, while the 3^{rd} order PCM model requires only 15 simulation runs for approximating the pdf of SDSCR with the same level of accuracy. The time taken from MCS is also almost 20 times larger than that from the PCM model for SDSCR.

3.4.3.2. Estimating SDSCR for Different Wind Penetration

Further, the proposed approach is used to analyze the effect of uncertain wind generation on grid strength. SDSCR is estimated when wind power penetration is increased from 20% to 40% of total load power in the system. Fig. 3.5 shows the cdf of SDSCR at bus 2 for different wind penetrations based on the 3rd order PCM model. Table 3.4 shows the statistic results.

It is observed from Fig. 3.5 and Table 3.4 that the increasing penetration of wind power leads to more uncertain behaviors affecting the grid strength. As shown in Fig. 3.5, the values for SDSCR lies approximately between 2.5 and 15 for lower wind power penetration (i.e., 20%

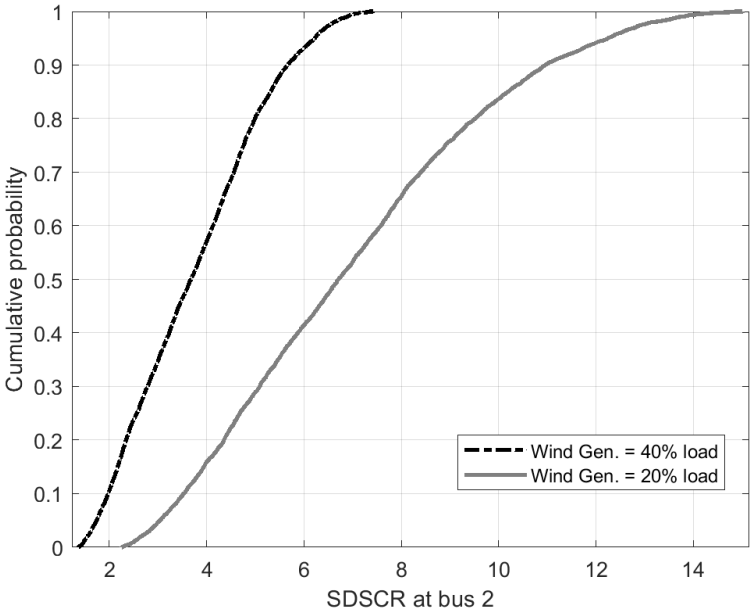

Figure 3.5. Cumulative distribution function (cdf) plot for SDSCR at bus 2 with different wind power penetrations using the 3^{rd} order PCM model.

Table 3.4. Statistics for SDSCR with different wind power penetration using 3^{rd} order PCM model

Wind Generation	40% of total load (150 MW)	20% of total load (75 MW)
mean	3.7488	6.9966
variance	1.9419	7.8545

penetration), whereas for higher wind penetration (i.e., 40% penetration) SDSCR lies between 1.5 to 7.5. This indicates that the risk of weak grid conditions increases with the penetration of wind generation. Also, Table 3.4 shows that the means and variances for SDSCR has reduced after increasing the wind penetration. This implies that the increasing penetration of uncertain wind power has significant impact on grid strength. The proposed approximation method can quantify the uncertainty impact on grid strength by calculating the means and variances of SDSCR under uncertain renewable generation.

3.5. Probabilistic Approximation Method for Grid Strength Assessment Power Grid Integrated with Solar Energy

The grid strength of a power grid is increasingly affected by the uncertain behavior of IB-RERs. To quantify the change of the grid strength under intermittent renewable generation, the ESDSCR-based method is integrated with the PCM, which models the impact of uncertain renewable generation probabilistically based on their historical data and evaluates the probabilistic results instead of deterministic values.

3.5.1. Probabilistic Model of Solar Power Generation

The historical or the predicted data unique to the installation site can demonstrate the uncertainty characteristic of renewable generation. Here, the uncertain parameter is taken as PV generation, which is a function of the PV irradiance. Thus, the effect of PV irradiance on the ESDSCR metric of grid strength is discussed and evaluated. The forecasted or the historical data for PV irradiance can be used for probabilistically modeling the intermittent nature of PV generation. The actual PV irradiance data from 2015 to 2020 retrieved from the NREL database [47] to accurately represent the probability models of PV irradiance. Like in many studies [19], the variation of irradiance data is modeled as beta distribution. For example in Fig. 3.6, the beta distribution is used to fit the histogram of the five years long raw data of PV irradiance at 12 pm. The shape parameters a and b from the beta distribution fit are obtained as 2.3318 and 2.1218 respectively, which is used to represent the irradiance distribution of solar farms. Here, the probabilistic modeling of the input PV irradiance is treated as independent probability distributions. Equation (3.19) represents the pdf for solar irradiance.

$$pdf(\xi) = \begin{cases} \frac{\Gamma(a+b)}{\Gamma(a)\Gamma(b)} \times \xi^{(a-1)} \times \\ (1-\xi)^{(b-1)}, & \text{for } 0 \leq \xi \leq 1, a \geq 0, b \geq 0 \\ 0, & \text{otherwise} \end{cases} \tag{3.19}$$

where ξ is solar irradiance in kW/m^2, $\Gamma(.)$ is the Gamma function, and a and b are parameters of the beta pdf.

The power generated from a PV module depends on solar irradiance, ambient temperature and the module characteristics [16]. The equations in (3.20) are used to find the power generated

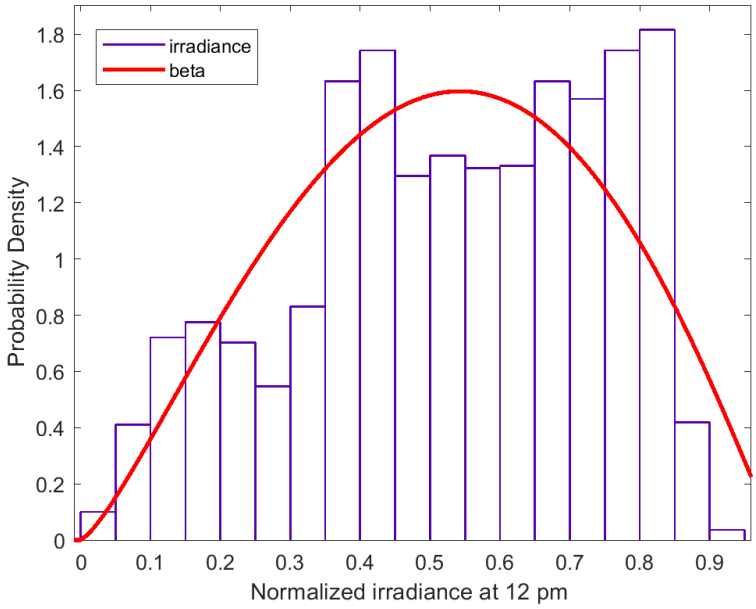

Figure 3.6. Beta distribution fit for solar irradiance at 12 pm of NREL data.

by the PV plant [48]. Note that the PV cell temperature is neglected.

$$P_{PV}(\xi) = \begin{cases} P_R\left(\frac{\xi^2}{\xi_{std}\xi_c}\right), & 0 < \xi < r_c \\ P_R\left(\frac{\xi}{\xi_{std}}\right), & \xi > r_c \end{cases} \tag{3.20}$$

where ξ_{std} is the solar irradiance in standard environment (1000 W/m^2), ξ_c is the minimum solar irradiance (150 W/m^2), and P_R is the rated output power of the PV farm.

To derive the orthogonal polynomials of the PV irradiance for the application of the PCM, we consider Jacobi polynomial which is orthogonal over [-1,1] with respect to the weighting function $(1-x)^\alpha(1+x)^\beta$ with $\alpha > -1$ and $\beta > -1$.

$$\int_{-1}^{1} P_i(x)P_j(x)(1-x)^\alpha(1+x)^\beta dx = 0, \quad i \neq j \tag{3.21}$$

The weight function for Jacobi polynomials can be rearranged to represent the density function of a beta distribution [49]. The orthogonal polynomials for the representative distribution can be derived by the method described in [50]. Equation (3.21) can be rearranged by comparing it with the Jacobi polynomials and is written as in terms of y as a transitional variable in the equation

given below:

$$\int_0^1 P_i(1-2y)P_j(1-2y)(y)^{\alpha}(1-y)^{\beta}dy = 0, \quad i \neq j \tag{3.22}$$

In (3.22), $x = 1-2y$ and y is a random variable with the parameters for beta distribution is $\alpha+1$ and $\beta+1$. Using (3.22) and the Gram-Schmidt process [51], the orthogonal polynomials for the PV irradiance for the solar generators can be derived. These orthogonal polynomials are used to obtain the collocation points in the traditional method and to build the approximation model for grid strength in terms of irradiance.

To demonstrate the use of k-means clustering method to obtain the collocation points, Fig. 3.7 shows the outcome of k-means clustering method used in the PV irradiance at 12 pm for NREL data shown in Fig.3.6. The PV irradiance is divided into six clusters and it can be seen that each cluster centroid (denoted as $\mathbf{X}$) represents the range of irradiance data of each cluster. The cluster centroids obtained are $\{179.83,\ 403.61,\ 528.95,\ 665.89,\ 791.15,\ 909.06\}\ W/m^2$, that are utilized as collocation points for model runs to determine the coefficients of the approximation model.

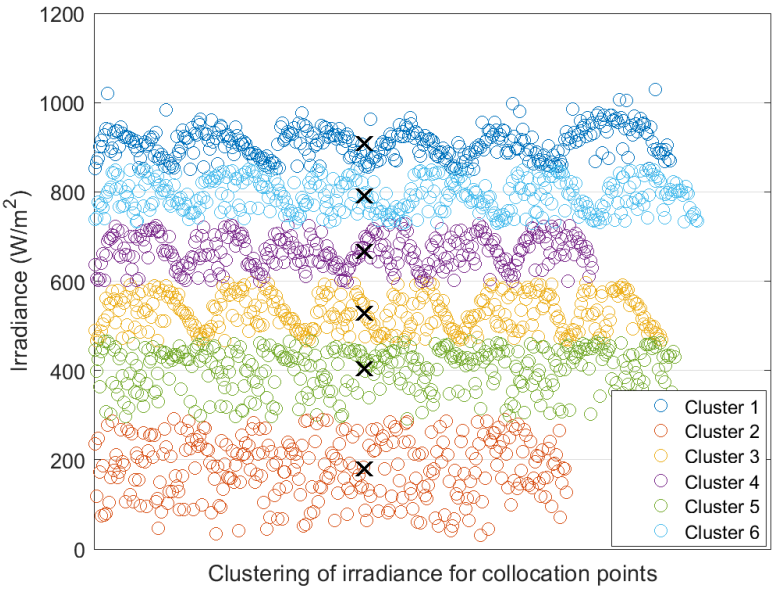

Figure 3.7. Clusters of solar irradiance using k-means clustering method.

3.5.2. Probabilistic Evaluation of ESDSCR

Fig. 3.8 presents the flowchart for generalized approach for probabilistically evaluation of grid strength of power system. A detailed approach for assessing grid strength quantified in terms of ESDSCR under uncertain solar generation using the PCM can be summarized as follows:

1. Obtain the actual historical/predicted data of uncertain input parameters such as solar irradiance, solar power generation and convert into intermediate variable using (3.21)-(3.22) to obtain appropriate pdf of uncertain parameters. Evaluate orthogonal polynomial functions from the obtained pdf based on equations (2.1)-(2.3).

2. Develop the polynomial models of the ESDSCR metric (output response) with respect to uncertain input variables of corresponding solar irradiance in step 1) using (2.5) or (2.9) and unknown coefficients.

3. Compute the collocation points using k-means clustering method and run power flow calculation at these points to find the corresponding output response of ESDSCR defined in (3.5).

4. Utilize these collocation points calculated and the corresponding output of ESDSCR in step 3) to obtain the unknown coefficients of the approximation model for ESDSCR developed in step 2) to assess grid strength under uncertain solar generation.

3.5.3. Comparison of K-means Clustering and Traditional Root Methods

The efficacy of the K-means clustering method for collocation points selection is demonstrated on the modified IEEE 9-bus system as shown in Fig. 3.9, where two synchronous generators at buses 1 and 2 are replaced with two solar farms with 100 MW and 50 MW rated power respectively. The parameters of the beta pdf for these solar farms are obtained from the fitting of the irradiance at 12 pm and 1 pm of NREL data. The values of the parameters for the beta pdf and the orthogonal polynomials for the respective irradiance of the solar farms are listed in Table 3.5, where $H_i(y_1)$ represents the orthogonal polynomials for solar farm 1 and $G_i(y_2)$ for solar farm 2. The roots from $H_i(y_1)$ and $G_i(y_2)$ is later converted back to relevant solar irradiance.

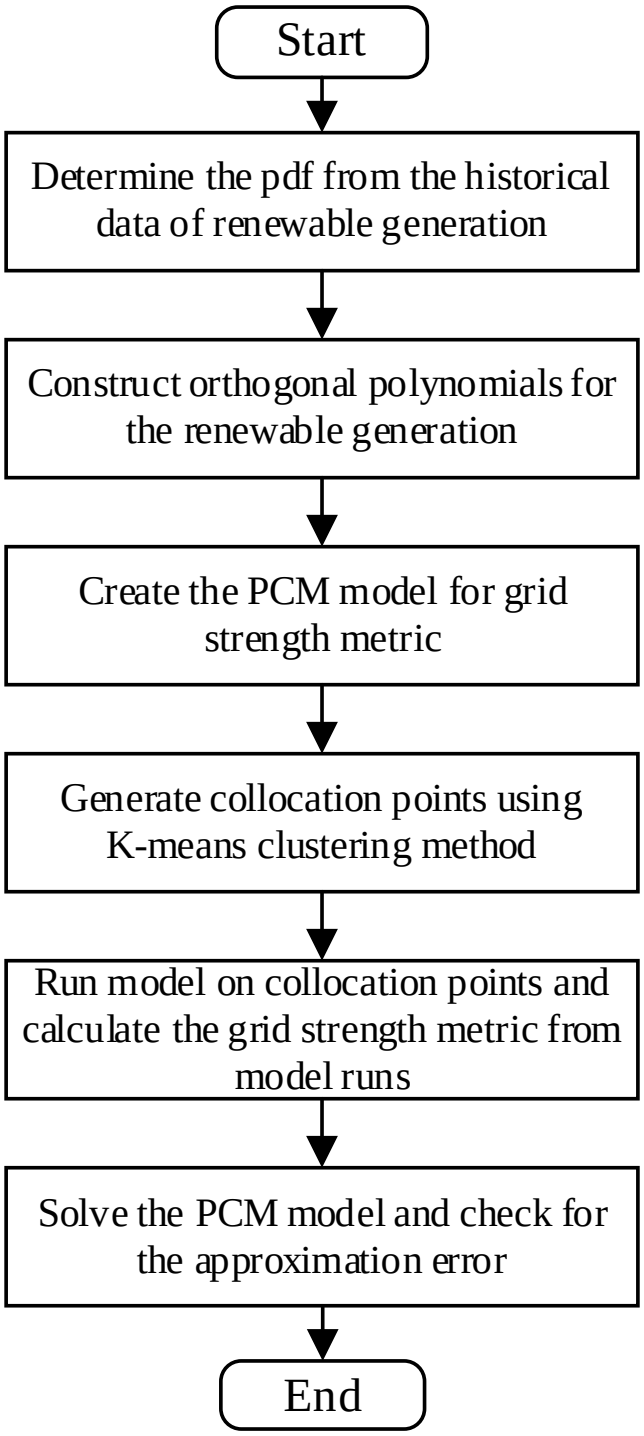

Figure 3.8. Flowchart of probabilistic approximation method for grid strength assessment.

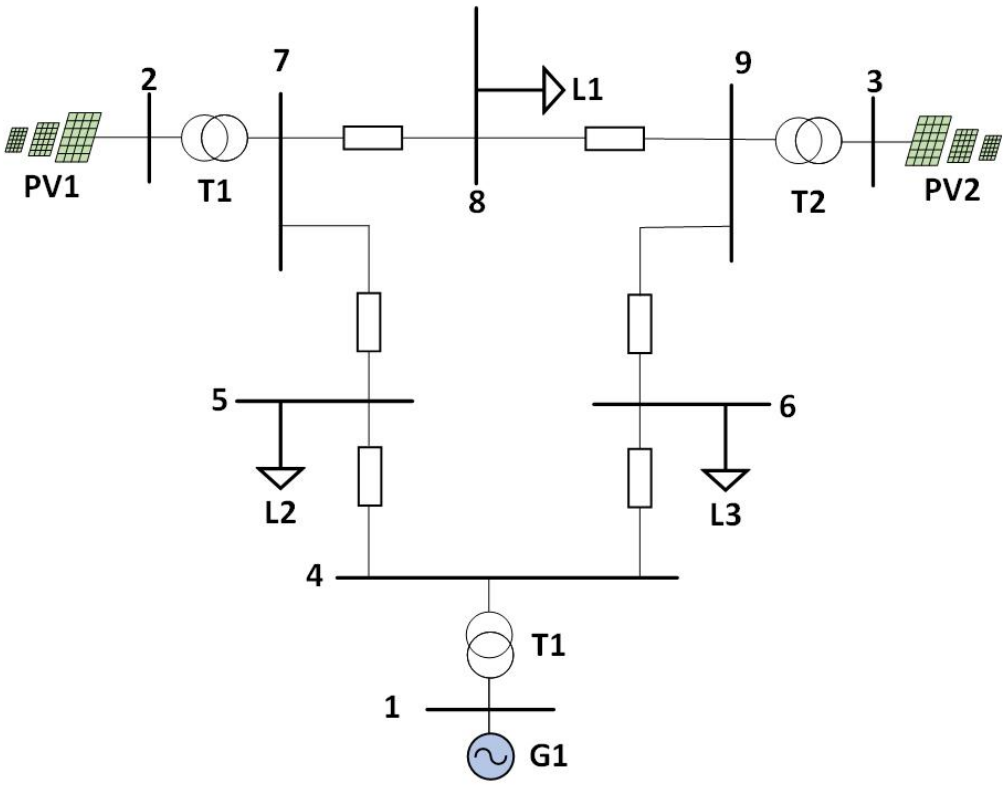

Figure 3.9. Modified IEEE 9 bus system with two solar farms.

Table 3.5. Parameters and 0rthogonal polynomials for solar farms

Solar farm 1 ($a = 2.33$ &$b = 2.12$)
$H_1(y_1) = 2.225y_1 + 0.105$
$H_2(y_1) = 4.3940{y_1}^2 + 0.28612y_1 - 0.8007$
$H_3(y_1) = 8.4592{y_1}^3 + 0.6306{y_1}^2 - 3.3886y_1 - 0.1019$
$H_4(y_1) = 16.1893{y_1}^4 + 1.3013{y_1}^3 - 10.2355{y_1}^2 - 0.4775y_1 + 0.6835$
...
Solar farm 2 ($a = 2.12$& $b = 1.71$)
$G_1(y_2) = 1.915y_2 + 0.205$
$G_2(y_2) = 3.5198{y_2}^3 + 0.4950y_2 - 0.7077$
$G_3(y_2) = 6.4954{y_2}^3 + 1.0203{y_2}^2 - 2.7918y_2 - 0.1821$
$G_4(y_2) = 2.0883{y_2}^4 + 2.0167{y_2}^3 - 8.0735{y_2}^2 - 0.7969y_2 + 0.5790$
...

Table 3.6. Comparison of K-means clustering and Traditional root methods for collocation point selection

Bus	PCM Order	MCS		K-means clustering				Traditional root			
		μ	σ^2	μ	σ^2	e_{SSR}	e_{RSSR}	μ	σ^2	e_{SSR}	e_{RSSR}
2	1	3.4492	1.9004 -	3.7476	1.9864	2.0328	0.5369	4.311	2.5921	**1.4852**	**0.233**
	2			3.7808	1.8801	**1.1204**	**0.2989**	4.1196	5.6155	3.5225	0.9898
	3			3.9063	1.9676	1.3494	0.3454	3.9158	5.2074	3.2401	0.8274
3	1	3.4833	1.1109	3.7459	3.5633	1.8204	0.4247	5.0513	1.582	**1.3685**	**0.2709**
	2			3.6414	1.8314	1.5933	0.4047	4.2772	5.0636	3.4023	0.8688
	3			3.6646	1.7691	**1.1959**	**0.3281**	3.7756	5.2028	2.757	0.7302

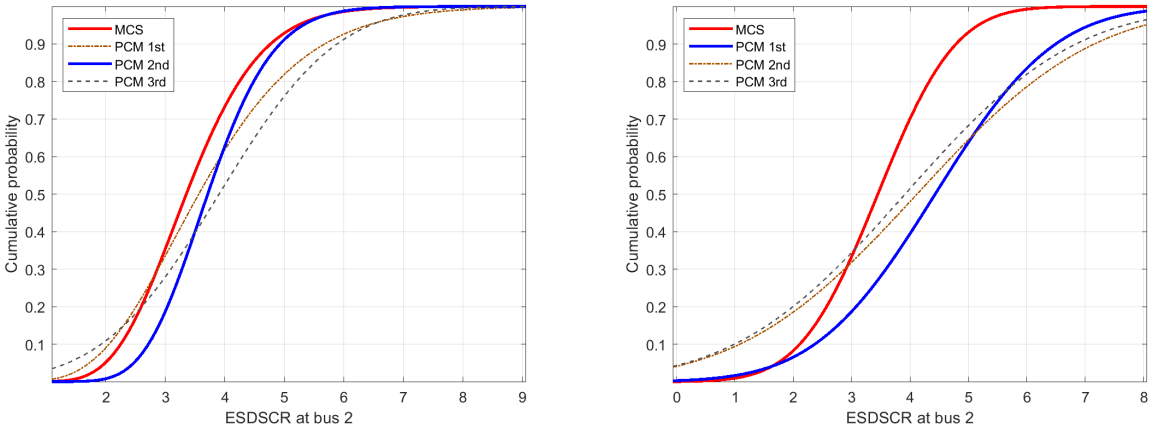

(a) K-means clustering (b) Traditional root

Figure 3.10. Cumulative probability plots for different selection methods for collocation points for ESDSCR at bus 2

The approximation using the collocation points generated by K-means clustering method are compared with the approximation obtained using the roots of these orthogonal polynomials [4, 12] and with the results from MCS with 10,000 simulation runs. The sum- squared-root error (e_{SSR}) is computed as an index for quantifying the approximation accuracy [22] and is given by,

$$e_{SSR} = \sqrt{\frac{\sum_{i=1}^{\eta} (\hat{Y}_i - Y_i)^2 f(\vartheta_i)}{\eta f(\hat{\vartheta})}} \tag{3.23}$$

where Y_i is the actual output from the simulation run, $\hat{Y}_i$ is the estimated output, η is the collocation points, $f(\vartheta_i)$ is the joint pdf and $f(\vartheta)$ is the pdf of the highest probability collocation point. The relative sum-squared-root error (e_{RSSR}) can also be computed as normalized version [52],

$$e_{RSSR} = \frac{e_{SSR}}{\mu(\hat{Y})} \tag{3.24}$$

where $\mu(\hat{Y})$ is the mean value of $\hat{Y}$.

In this comparison study, the PCM approximation model for ESDSCR at buses 1 and 2 with different orders (1^{st} – 3^{rd} order) are derived using collocation points obtained from K-means clustering method and traditional root method and compared with MCS results. The approximation errors for each order of approximated model for both methods are calculated based on (3.23)

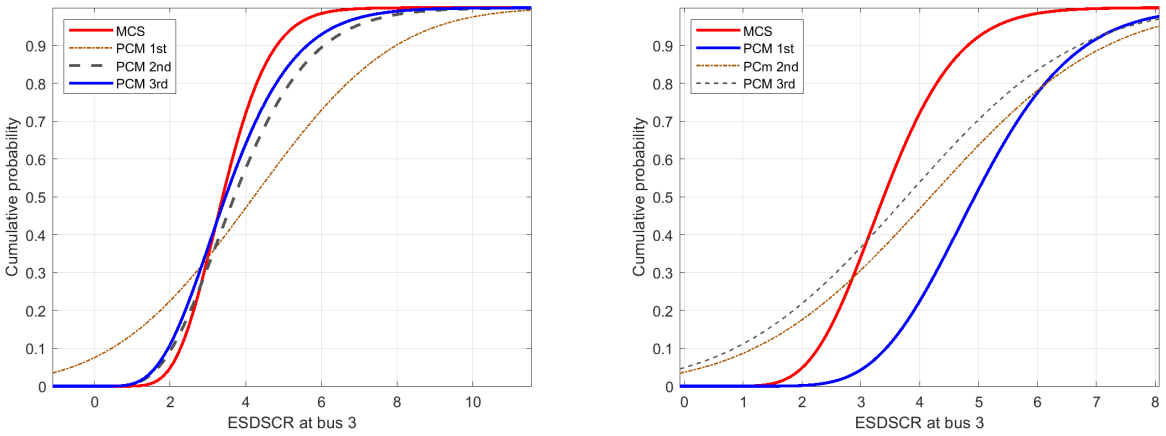

(a) K-means clustering

(b) Traditional root

Figure 3.11. Cumulative probability plots for different selection methods for collocation points for ESDSCR at bus 3

and (3.24). Fig. 3.10 and Fig. 3.11 shows the cumulative distribution function (cdf) curves from MCS and the approximation models of three different orders for ESDSCR at bus 2 and 3 using k-means clustering and traditional root methods. Table 3.6 compares the errors, the mean value, and the variance value of MCS method and three different orders of PCM method for ESDSCR at bus 2 and 3 using k-means clustering and traditional root methods.

From Fig. 3.10a, it can be observed that the 2^{nd} approximation model provides better estimation of ESDSCR at bus 2 than the 1^{st} and 3^{rd} order models using k-means clustering method for determining the representative simulation points from the distribution of the uncertain solar irradiance. However, when roots of higher orders (traditional root method) was used for collocation point for PCM modeling, as seen in Fig. 3.10b, 1^{st} order approximation model fits better than its higher counterparts. Further, it can be seen in Table 3.6, the errors for 2^{nd} order approximation model using k-means clustering is the lowest (i.e. e_{SSR}=1.1204 and e_{RSSR}=0.2989) than the other two orders. Similarly, for traditional root method 1^{st} order model has the lowest errors of e_{SSR}=1.4852 and e_{RSSR}=0.233 than the remaining models. Thus, for estimation of ESDSCR at bus 2, 2^{nd} order approximation obtained using k-means clustering is preferred, whereas 1^{st} order approximation model is better for estimation using traditional root method. It can be further observed that the means and variances from the 2^{nd} order PCM model using k-means clustering (i.e.

μ=3.7808 and σ^2=1.8801) are much closer to those from MCS (i.e. μ=3.4492 and σ^2=1.9004) than the approximation model using traditional root method (i.e. μ=4.3110 and σ^2=2.5921).

Similar observations can be detected from the cdf plots of ESDSCR at bus 3 for both the selection methods in Fig. 3.11 and Table 3.6. The cdf plot in Fig. 3.11a and the errors of e_{SSR}=1.1959 and e_{RSSR}=0.3281 in Table 3.6 indicate that 3^{rd} approximation model estimates the better ESDSCR for bus 3 using k-means clustering as point selection method. For traditional method, ESDSCR at bus 3 was approximated better using 1^{st} order PCM model with least errors. The mean obtained from model using k-means method (i.e. 3.6646) matches the mean of 3.4833 from MCS method, whereas the mean from model using traditional root (i.e. 5.0513) is quite different. According to these observations, the approximation model using k-means clustering method yields better selection of the collocation points to provide more accurate estimation compared with the traditional root method.

Table 3.7. Computational time (sec) for different methods

PCM Order	1	2	3
MCS		102.71	
K-means clustering	0.69	1.09	2.58
Traditional root	1.88	2.11	2.89

It can be seen from Table 3.7 that the PCM modeling using any selection methods, k-means clustering or traditional root, saves substantial amount of computational time compare to that from MCS. Note that the computational time for k-means clustering is slightly lesser than that of traditional root but not significant enough as both these methods require equal number of simulation runs for approximating the PCM model to obtain similar accuracy of MCS results. Therefore, k-means clustering method for selection of collocation points is further used in a larger model since it is more accurate and equally computationally efficient than the traditional root method.

3.5.4. Estimating ESDSCR using PCM in IEEE 39 bus system

The proposed method for grid assessment is demonstrated using modified IEEE 39 bus system with solar farms integrated in the test system, as shown in Fig. 3.12, by comparison of the ESDSCR at different buses approximated using PCM and MCS of irradiance data from the Baseline

Table 3.8. Parameters for solar farms

Bus		30	35	36	37	38	39
Rated power (MW)		250	650	560	540	830	1000
Parameters	a	2.33	2.07	2.01	1.74	2.12	2.14
	b	2.12	2.37	3.35	4.80	1.71	1.71

Measurement System of the Solar Radiation Research Laboratory of NREL [53]. The synchronous generators in different buses are replaced by solar farms and the irradiance at different time period (e.g. at 12 pm, 1 pm, etc.) are used in the solar farms as irradiance data for diversity of irradiance in each farm. The beta distribution is used to fit the raw irradiance data for different time period and the parameters obtained, as shown in Table 3.8, are used to define the pdf of irradiance for the solar farms.

The beta distributed irradiance parameters $(\xi_1, \xi_2, ..., \xi_6)$ is rearranged using Jacobi polynomials (3.22) to find the orthogonal polynomials using the Gram-Schmidt process [51] and recursive formula described in [50]. The orthogonal polynomials determined for two of the solar farms can be referred from Table 3.5. The collocation points are determined using k-means clustering method and used to find the coefficients of the (1^{st}-3^{rd}) orders approximation model for ESDSCR using (2.6).

3.5.4.1. PCM Simulation in Various Orders

The ESDSCR values for all the buses where PV is integrated are estimated using the proposed method and MCS. Table 3.9 presents the means and variances obtained from the (1^{st}-3^{rd}) orders PCM model and MCS. The errors for the approximation models are calculated using (3.23) and (3.24) for each estimation and presented in Table 3.9. For illustration, the cdf plot and pdf plot for the ESDSCR estimation at buses 36 and 38, using three different approximation models and MCS is shown in Fig. 3.13 and Fig. 3.14 respectively. It can be observed from Fig. 3.13 that the 2^{nd} order approximation model provides a better estimation of ESDSCR at bus 36 than the 1^{st} or 3^{rd} order PCM models with probabilistic values of solar generation. Moreover, Table 3.9 shows the means and variances od ESDSCR at bus 36 from the 2^{nd} order PCM model (i.e., 1.68 and 1.93) are closer to those from MCS (i.e., 1.95 and 1.17) than those of the 1^{st} or 3^{rd} order PCM models. Besides the statistics, the errors for 2^{nd} order approximation (i.e., e_{SSR}= 1.11 and e_{RSSR}= 0.55)

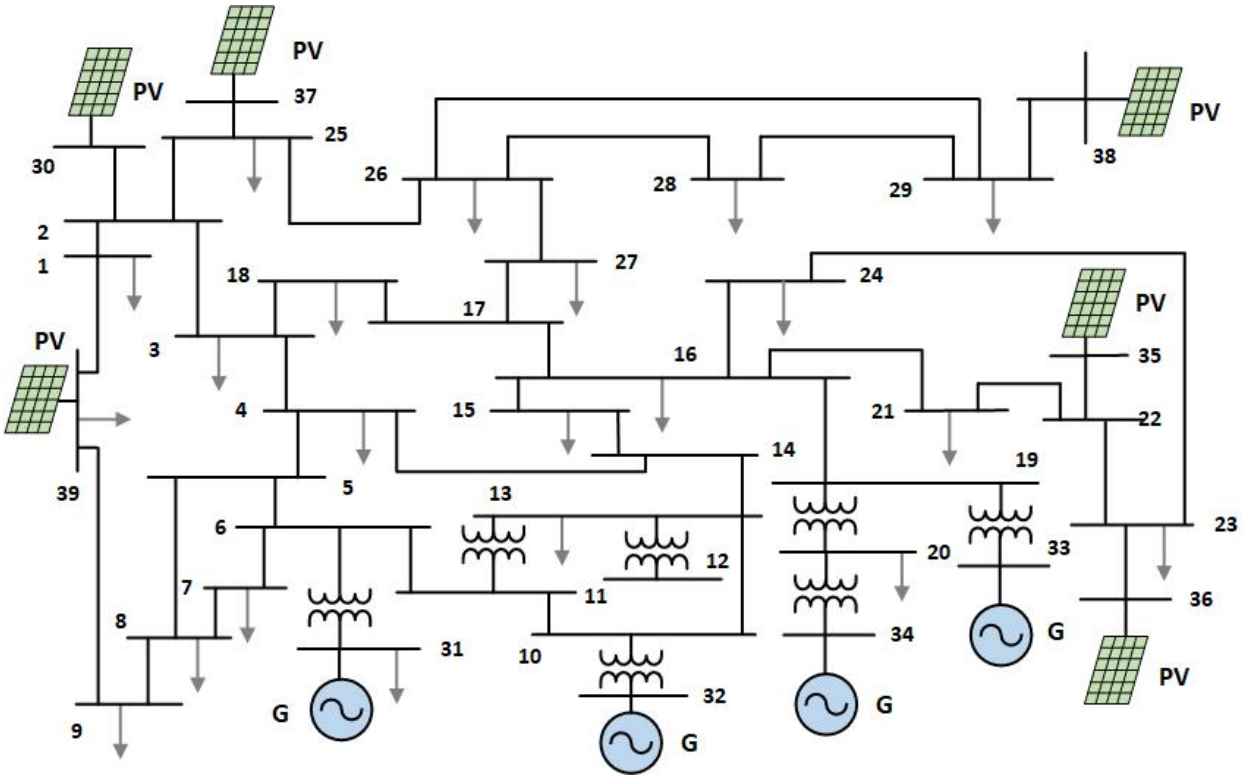

Figure 3.12. Modified IEEE 39 bus system with six solar farms.

are lower than that of other orders. Thus, the 2^{nd} order PCM approximation model provides a better estimation of ESDSCR at bus 36.

Likewise, Fig. 3.14 and Table 3.9 shows that the ESDSCR at bus 38 is better estimated using 1^{st} order approximation than the higher order models.The means and variances of 1^{st} PCM model (i.e. 1.4250 and 0.8721) align better with the MCS results (i.e. 1.5875 and 1.7533) compared to the higher order PCM models. The errors (i.e., e_{SSR}= 1.28 and e_{RSSR}= 0.21) are the lowest for 1^{st} PCM model, which further proves accuracy in estimation. The means and variances for the approximation model of each bus that matches closest to that of MCS is highlighted in Table 3.9 to indicate the order of the PCM model that provides the most accurate results. Furthermore, it is well established that the proposed method for probabilistic grid strength assessment can save a substantial amount of simulation runs and computational time compared with traditional MCS. For example, it takes 7 sets of collocation points to model a 1^{st} order PCM, 28 sets of points for 2^{nd} order PCM model, and so on, whereas it requires 10,000 simulation runs in MCS for approximating the probability distribution of ESDSCR at a bus with the same level of accuracy.

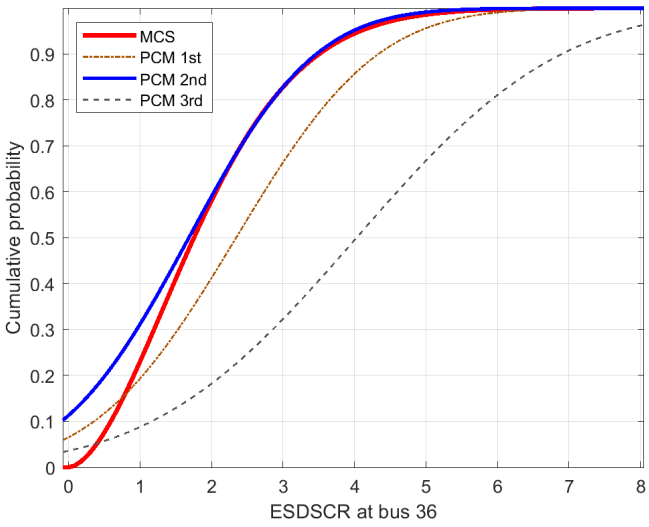

Figure 3.13. Cumulative distribution plot of MCS and different orders of PCM models of ESDSCR at bus 36.

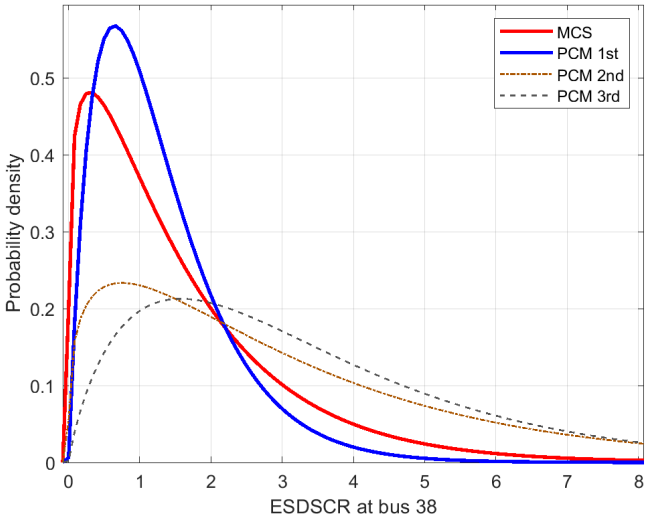

Figure 3.14. Probability density plot of MCS and different orders of PCM models of ESDSCR at bus 38.

Table 3.9. ESDSCR using MCS and PCM for different PV buses

PV Bus	MCS		PCM 1				PCM 2				PCM 3			
	μ	σ^2	μ	σ^2	e_{SSR}	e_{RSSR}	μ	σ^2	e_{SSR}	e_{RSSR}	μ	σ^2	e_{SSR}	e_{RSSR}
30	2.0681	1.5312	**2.1071**	**1.6784**	2.02	0.94	3.9650	3.5580	5.28	1.33	1.8793	2.5212	3.61	1.92
35	2.0282	1.2307	**2.2734**	**2.7818**	2.63	1.16	2.9056	4.1963	3.07	0.77	3.4012	4.3138	4.03	1.17
36	1.9577	1.1788	2.3340	2.4068	1.31	0.65	**1.6838**	**1.9329**	1.11	0.55	4.0286	5.008	3.74	0.93
37	2.0276	1.6170	3.5284	4.2343	1.77	0.51	**2.7069**	**4.8220**	1.52	0.56	3.6152	5.261	2.99	0.82
38	1.5875	1.7533	**1.4250**	**0.8721**	1.28	0.21	2.4591	4.921	1.89	0.59	3.4240	3.8610	2.68	0.78
39	1.5794	1.7632	**2.7862**	**1.0382**	1.81	0.65	2.885	3.7702	1.37	0.44	2.9473	3.4564	2.41	0.82

3.5.4.2. Estimating ESDSCR for Different PV Penetration

Further, the proposed approach is used to analyze the effect of uncertain solar generation on grid strength. In this case study, ESDSCR is estimated for different solar power penetration with respect to total load power in the system. Fig. 3.15 shows the range of ESDSCR at bus 38 for different PV penetrations based on the 1^{st} order approximation and the statistic results are given in Table 3.10. From Fig. 3.15 and Table 3.10, it is evident that the increasing penetration of solar power leads to more uncertain behaviors affecting the grid strength. The range of ESDSCR values lies below 3.21 for higher PV power penetration (i.e., 60% penetration) which reflects weak grid conditions as $ESDSCR < 3$. For 30% PV penetration, the median of the range lies at 2.74 which shows equal variability of the grid conditions and for 15% penetration, the 25^{th} percentile of ESDSCR values lies above 3.03, indicating mostly strong grid as $ESDSCR > 3$. This demonstrates that the risk of weak grid conditions increases with the higher penetration of solar generation. The means and variances also verifies decreasing range of ESDSCR (grid strength) with increasing solar penetration. Thus, this proposed approximation method serves as a great visualization tool that can quantify the uncertainty impact on grid strength under uncertain renewable generation and inform the power system planners of possible impacts.

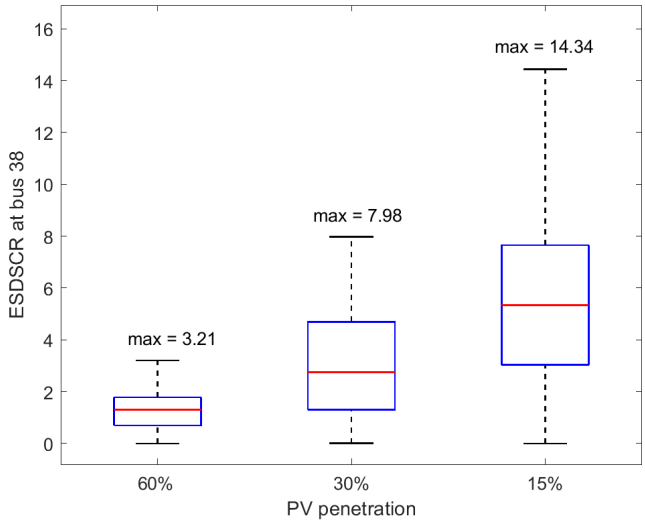

Figure 3.15. Boxplot for ESDSCR at bus 38 with different PV penetrations using 1^{st} order approximation.

Table 3.10. Estimation of ESDSCR with different PV penetration

PV Penetration	60%	30%	15%
μ	1.4250	3.1132	5.4869
σ^2	0.8721	2.1013	3.1678

3.6. Summary

This paper proposed a probabilistic approach for assessing grid strength of power systems under uncertain renewable generation by integrating the PCM with the SDSCR-based method. In the proposed approach, the SDSCR-based method and ESDSCR-based method are used for grid strength assessment, while the PCM was used to establish the approximation polynomial functions with multiple input variables for modeling the impact of uncertain renewable generation. The PCM is a computationally efficient technique, which can reduce the computation burden without compromising the result accuracy compared to traditional Monte Carlo simulation. Moreover, the traditional root mehtod was tested with K-means clustering method for selecting the most representative collocation points for accurate approximation. PCM-based method with K-means clustering technique was more accurate in estimating the grid strength of IEEE 9 bus sytem with two PV farms than the traditional root method for collocation point selection.

The efficacy of the proposed method with SDSCR metric is demonstrated on the modified IEEE 9-bus system with multiple renewable resources. Further, the proposed method with ESDSCR metric is tested with higher number renewables (six PV farms) on the modified IEEE 39-bus system. The distribution of the grid strength metirc with respect to the uncertainties of the renewable genration is determined and the range of the values of the metric can be predicted using the proposed method. Further, the results show that with higher penetration of renewables, the integration points in grid becomes more weak which increases the posibility of stability issues in the network. The proposed approach is promising for grid strength assessment while considering the impact of variable renewable generation to guide grid planning and operation for identifying potential weak grid issues.

4. IMPACT ANALYSIS OF TRANSMISSION-LEVEL DISTURBANCES ON SOLAR PV IN DISTRIBUTION SYSTEMS[1]

4.1. Introduction

The electric power grid is undergoing a rapid change driven by the high penetration of renewable energy resources such as solar and wind via power electronic inverters. While these inverter-based RERs (IB-RERs) can use power electronic controls to respond to grid disturbances nearly instantaneously and thus support grid reliability, they are challenging grid planning, operation, and protection [6]. The North American Electric Reliability Corporation (NERC) recently reported a series of similar events of the unintended loss of solar generation following the transmission-level disturbances that occurred from 2016 to 2020 in the Southern California region of the Western Electricity Coordinating Council's footprint [6, 7, 8, 9].

- On 16 August 2016, the transmission system owned by Southern California Edison experienced thirteen 500 kV line faults, and the system owned by the Los Angeles Department of Water and Power experienced two 287 kV faults as a result of the fire. The most significant event resulted in the loss of nearly 1200 MW. There were no solar PV facilities de-energized as a direct consequence of the fault event; rather, the fa-cilities ceased output as a response to the fault on the system [6].

- On 9 October 2017, the fire caused two transmission system faults near the Serrano substation, east of Los Angeles. The first fault was a normally cleared phase-to-phase fault on a 220 kV transmission line, and the second fault was a normally cleared phase-to-phase fault on a 500

[1]This chapter is based on the work published as An RTDS-Based Testbed for Investigating the Impacts of Transmission-Level Disturbances on Solar PV Operation," *Energies 2021: Special Issue Power System Dynamics and Renewable Energy Integration* [54]. The authors of the paper are M. Maharjan,, A. Ekic, B. Strombeck and D. Wu. M. Maharjan was the first author and responsible for writing the manuscript, implementing the case studies for simulation results in PSCAD software, formal analysis and investigation of the results. A. Ekic developed the RTDS testbed and provided results for RSCAD software and helped in investigation of the results. B. Strombeck and Dr. D. Wu gave guidance on methodology, reviewed and wrote the manuscript.

kV transmission line. Both faults resulted in approximately 900 MW of solar PV generation loss [7].

- On 20 April 2018 and 11 May 2018, two similar events caused a loss of solar pho-tovoltaic (PV) facilities in response to transmission line faults, though no generating resources were tripped as a consequence of either of the line outages [8].

- On 7 July 2020, the static wire on a 230 kV double circuit tower failed, causing a single-line-to-ground fault on both the #1 and #2 parallel circuits on the tower. The fault was cleared normally in about three cycles. In addition, a nearby 230 kV line relay incorrectly operated for an external fault. For this first fault event, approximately 205 MW of power reduction was observed at solar PV facilities in the Southern California region. After the #1 circuit was re-energized and held, the #2 line was reenergized and relayed back out due to a low-impedance three-phase fault that was cleared normally in 2.3 cycles. This second fault event experienced a larger 1000 MW reduction in solar PV output primarily due to the fact that it was a three-phase fault [9].

These similar events highlight the potential reliability impacts of IB-RERs including solar PV systems at both the distribution and transmission levels. Recently, these events have been investigated in [55, 56, 57, 58, 59, 60, 61, 62, 63, 64, 65] [5–15]. To study the impact of IB-RERs on the bulk power systems, generic positive sequence dynamic stability simulations such as PSS/E are used with a simpler representation of IB-RERs and inverters in [55, 56, 57]. To more accurately capture the dynamics of the inverters' response to actual grid events using generic positive sequence stability models, reference [58] identifies the modeling deficiencies in generic inverter models. In [59, 60, 61], aggregated models of IB-RERs are used instead of individually detailed models of IB-RERs. Reference [62] presents a coupled simulation method, in which the transmission network is first initialized in a dynamic simulation platform and then the recorded response is passed to the distribution network, which is simulated in quasi-static time-series simulations. In [63, 64, 65], the impacts of inverter operating modes and inverter parameters on the transient stability of the bulk transmission system are studied. However, the existing works do not investigate the impact of the transmission-level disturbances on IB-RER operation, which is important for the operation of inverter-based resources. Additionally, these existing works usually use positive sequence stability

models and simple inverter modeling for simulation analysis. Such models may not be used in electromagnetic transient simulations for modeling intricate details with different inverter controls and accurately evaluating the IB-RERs' response during abnormal events. In addition, the complete network topology of the transmissions system and the distribution system is ignored, which cannot be used for understanding the characteristics of the transmission-level disturbances propagating into the distribution systems.

To address these issues, a real-time electromagnetic simulation testbed is constructed based on a Real-Time Digital Simulator (RTDS) by integrating an IEEE standard transmission network into an IEEE distribution test feeder interfaced with solar PVs in multiple locations in this paper. With the testbed and grid strength assessment, the impact of the transmission-level disturbances on solar PV operation is investigated under different fault types and locations, solar penetration levels, and loading levels.

The main contributions of this chapter can be summarized as follows:

1. To generate realistic transmission-level disturbances and investigate their impacts on solar PVs in distribution systems, a real-time electromagnetic simulation testbed is constructed based on RTDS, which is developed by RTDS Technologies Inc. to solve the power system equations fast enough to realistically represent conditions in actual power grids [66].

2. The testbed has a full model of a transmission system, distribution system, and solar PVs. In the modeling of solar PVs, the detailed PV inverter controls are considered in the distribution system with the comprehensive models of synchronous machines and excitation in the transmission system.

3. By using this testbed to investigate the impact of the transmission-level disturbances on solar PV operation under different fault types and locations, solar penetration levels, and loading levels, it is found that the grid strength at different POIs significantly affects the transient stability of solar PV operation. Particularly, at the weak POIs, undesirable transient stability events are more likely to occur under increasing solar penetration levels or decreasing loading levels following severe transmission-level disturbances.

The rest of the chapter is organized as follows: the detailed modeling of the testbed created using RTDS, including the transmission system, distribution system, and the PV systems and their inverter controls are presented and the validation of the model is done using PSCAD software with same parameters and models; the impact of transmission-level disturbances on solar PV operation in the distribution system is investigated by using the real-time testbed under different fault conditions, solar penetration, and loading levels, and additional discussion on the impact of grid strength on solar PV responses under different scenarios are presented; finally, a summary of the chapter is presented.

4.2. Real time Digital Simulator Based Testbed

4.2.1. Real Time Digital Simulator

To generate realistic transmission-level disturbances and investigate their impacts on solar PVs in distribution systems, a real-time electromagnetic simulation testbed is constructed based on RTDS, which is a commercially available digital real-time power system simulator. RTDS is developed by RTDS Technologies Inc. in Winnipeg, Canada, for the simulation and analysis of electromagnetic transients in electric power systems. RTDS can solve the power system equation fast enough to continuously produce output conditions that realistically represent conditions in actual power grids.

RTDS is generally composed of hardware and software, which is shown in Figure 1. The RTDS hardware includes processing and communicating cards, which are in-serted in the unit and connected to a common plate located in the back of the RTDS. The processing cards have a parallel processing architecture customized to simulate with one or multiple processors for the equation solution for the power system and its components. The communicating cards are used to handle the communication between RTDS and its software installed on the guest computer. RTDS has additional dedicated interface cards that allow the physical and logical connection between the simulated power systems and actual devices. The RTDS software is a graphic interface software, RSCAD, which allows users to build, compile, execute, and analyze simulation cases. This software has a wide library of power system components, control, and automated protection systems, as well as a friendly user interface, which can make the assembly and analysis of a wide variety of electric AC and DC systems easier and integrated. As shown in Fig. 4.1, users can use RSCAD software to build a model representing the power system and load this model to the RTDS for

the electromagnetic transient simulation while obtaining the updated states of the simulated power system model for analysis.

Figure 4.1. Real Time Digital Simulator (RTDS) testbed.

4.2.2. RTDS-Based Power System Model

With RTDS, a representative power system model is constructed for real-time electromagnetic simulations to investigate the impact of transmission-level disturb-ances on the IB-RER operation in distribution systems. This model includes complete transmission and distribution systems with solar PVs. Fig. 4.2 shows the single-line diagram of the constructed power system model. The component details in the model are described below.

4.2.2.1. Transmission System

In the RTDS-based representative power system model, the transmission system is demonstrated by the IEEE 9 bus test system. In the system, its voltages include 230 kV at the transmission level and generator bus voltages of 16.5 kV, 18 kV, and 13.8 kV at buses 1, 2, and 3. The system is composed of three loads, three transformers, six transmission lines, and three synchronous generators with exciter and governor con-trol systems. The system data can be found in [67]. The major electrical components used in the system include a hierarchy component box for the synchronous generator, the unified T-line model for the transmission line, and the dynamic load model.

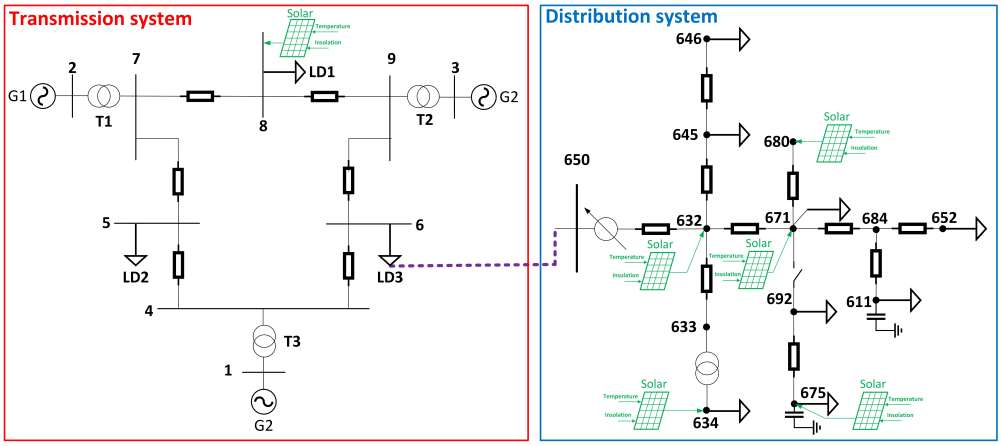

Figure 4.2. Single line diagram of the constructed model for real-time electromagnetic simulation.

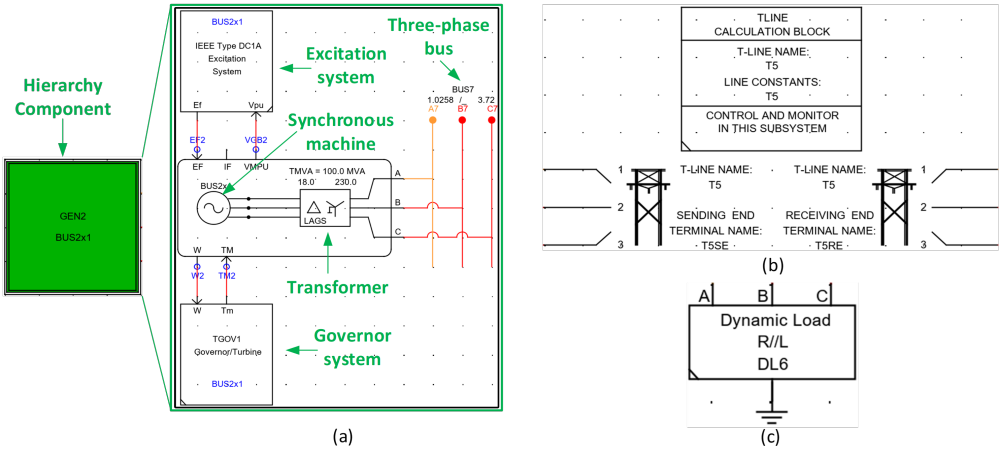

Figure 4.3. Modeling components used for constructing the transmission system in the real-time simulation testbed: (a) hierarchy component box for synchronous generator; (b) unified transmission line model; (c) dynamic load component.

- The synchronous generator and its excitation and governor systems are represented by a hierarchy component box. As shown in Fig. 4.3, this hierarchy component box includes the models of a synchronous machine and its excitation and governor systems. All the synchronous machine systems are modeled with a steam turbine, a governor system and an excitation system. The excitation system is modeled with an AC excitation type (EXAC1A) model. The time constants, regulators, and feedback gains are the input parameters for the excitation system. The machine is connected to the transmission system via a transformer.

- The transmission lines in the system are represented by the unified T-line model. As shown in F. 4.3, the unified T-line model is composed of three electrical components: sending end,

terminal end, and calculation box. The unified T-line model can be used for a Bergeron or a frequency-dependent phase model, but when required, either of these models can be collapsed into a simpler PI representation of a line. It is noted that in [59], the data are compensated for long line effects. The transmission lines in the RTDS simulation case are modeled using the Bergeron line model, which is simulated using distributed line parameters. Thus, the long line compensation was removed [65] to obtain the uncompensated data for the developed model.

- The load is represented by a dynamic load component in the transmission side of the network, which is shown in Fig. 4.3. The load model can be used to dynamically adjust the load to maintain real power and reactive power set points using variable conductance. Additionally, this model allows setting up the initial values and limits of real and reactive power absorbed by a load.

4.2.2.2. Distribution System

In the RTDS-based representative power system model, the distribution system is modeled by the IEEE 13 bus test feeder, which includes a two-winding transformer model, the PI section line model, dynamic load model, and a hierarchy component box for the voltage regulator [68].

- In this system, a delta-wye transformer is connected to the transmission system, and it is represented by a two-winding, three-phase transformer model, which is shown in Fig. 4.4.

- The distribution line is represented by the PI section model in which a set of PI sections are connected in series, as shown in Fig. 4.4. It is noted that the PI sec-tion model requests the capacitance from the wire to the ground. The data given in [69] are the shunt capacitance matrix. Thus, the capacitance from the wire to the ground needs to be calculated from this matrix.

- The load in the system is represented by hierarchy component boxes. As shown in Fig. 4.4, different colored hierarchy component boxes include different connections of loads, which are modeled by the dynamic load component.

The voltage regulator has been adopted from the typical parameters used for the IEEE 13 bus test feeder. The voltage regulator is represented by a hierarchy component box. As shown in

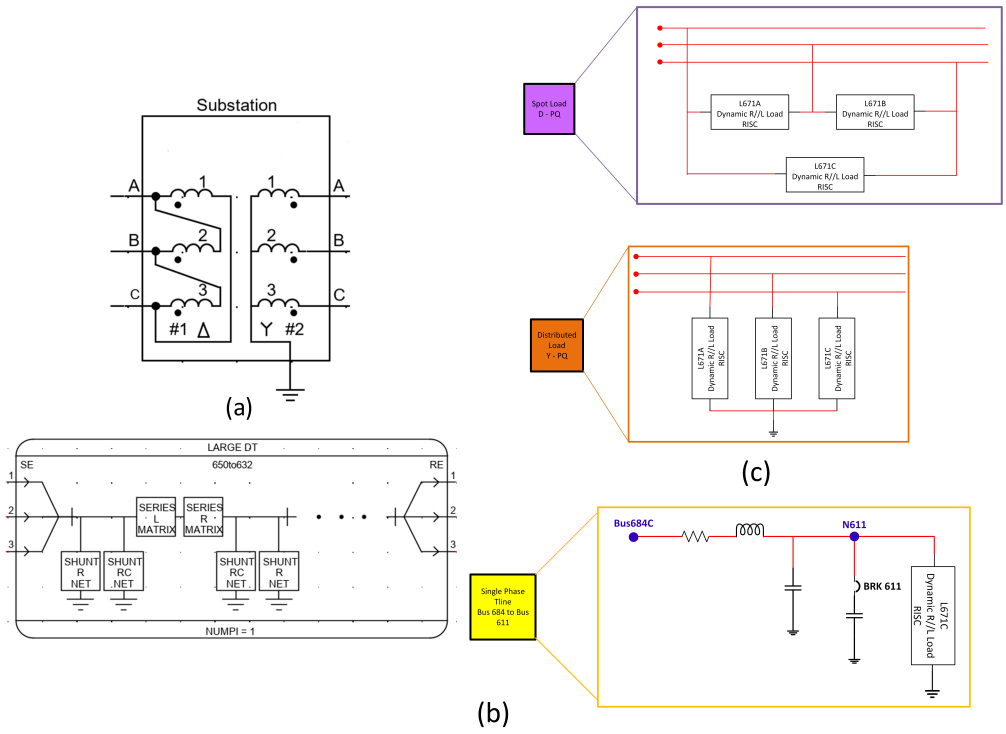

Figure 4.4. Modeling components used for constructing the distribution system in the real-time simulation testbed: (a) two-winding, three-phase transformer model; (b) PI section model for distribution lines; (c) hierarchy component boxes for loads.

Fig. 4.5, this hierarchy component box includes three single-phase two-winding transformers and the controls for the voltage regulator. For each phase, the regulator controls are represented by an individual hierarchy component box, in which there are the compensator circuit and the step voltage regulator control. This regulator is constructed based on reference [70].

4.2.2.3. Solar PV System

Solar PVs are integrated into the constructed transmission–distribution model. Each solar PV is modeled by the PV array component to supply the DC voltage for the converter. The converter is modeled using an average value model (AVM), and the AC side of the converter is connected to the feeder. Fig. 4.6 shows the solar PV modeling components.

- A PV array model is used to represent the combination of individual solar cells into PV arrays to produce voltages and currents at the terminals of a PV array. The PV array generates power as a function of irradiation and temperature. The parameters of the PV array model can be modified to obtain a certain output power for the given irradiation and temperature. Each PV

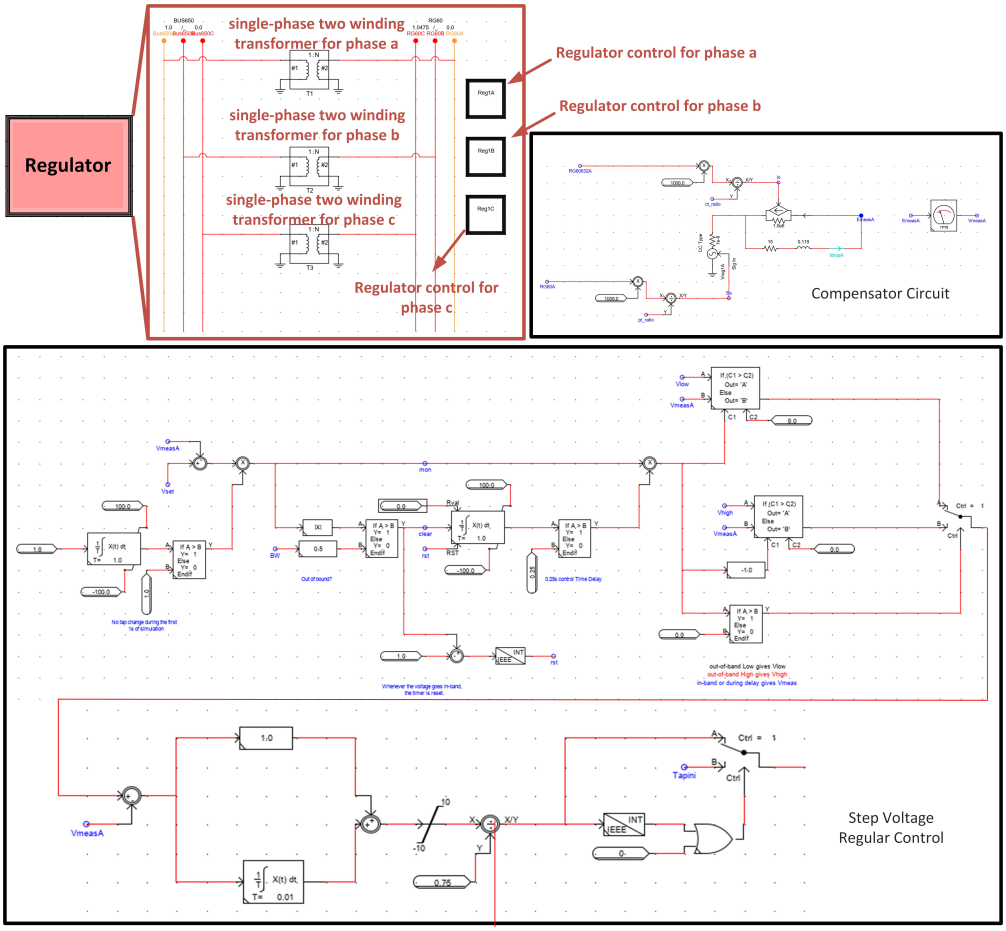

Figure 4.5. Voltage regulator used for constructing the distribution system.

array has a temperature set to 25 °C and insolation to 1000 W/m2 as input. This model can specify the parameters about how the cells are connected to form arrays. Additionally, this model can select different methods for estimating the maximum power point for a given insolation and temperature. The detailed parameters of the PV array are presented in Table 4.1.

- The AVM component models the averaged converter control dynamics developed by equivalent voltage and current sources. As shown in Fig. 4.7, solar PV controls use the maximum power point tracking (MPPT) algorithm, which computes the DC voltage set point required for maximum power transfer based on the temperature and insolation levels of the PV array. This DC voltage set point then feeds into the outer loop DC-bus voltage control, which computes a corresponding real power set point. The real and reactive power is then fed into the inner current control loop operating in the dq reference frame and a set of three-phase

Table 4.1. Parameters for solar PV system.

Components	Parameters	Value
PV	Number of series cells	36
	Number of parallel strings	1
	Open-circuit voltage (V_{oc})	21.7 V
	Short-circuit current (I_{sc})	3.35 A
	Number of modules in series	115
	Number of modules in parallel	285
	Voltage at Pmax	17.4 V
	Current at Pmax	3.05 A
DC link capacitor	Capacitance (C_{dc})	5 mF
Inverter	Filter resistance	1.0 mΩ
	Filter inductance	100 μH
High-pass filter	R_H	0.039 Ω
	L_H	7.874 μH
	C_H	2500 μF
Current control loop	k_{pi}	0.2
	k_{ii}	0.30675
PLL	k_{pPLL}	5
	k_{iPLL}	0.01

modulation waveforms is synthesized. These modulation waveforms are then used in a carrier-based, sinusoidal pulse width modulation (SPWM) strategy to generate a corresponding set of firing pulses.

4.3. Validation of RTDS-Based Power System Model

To verify the performance of the transmission-distribution model, described in the earlier section, the steady state and dynamic responses from the model developed in RSCAD software are

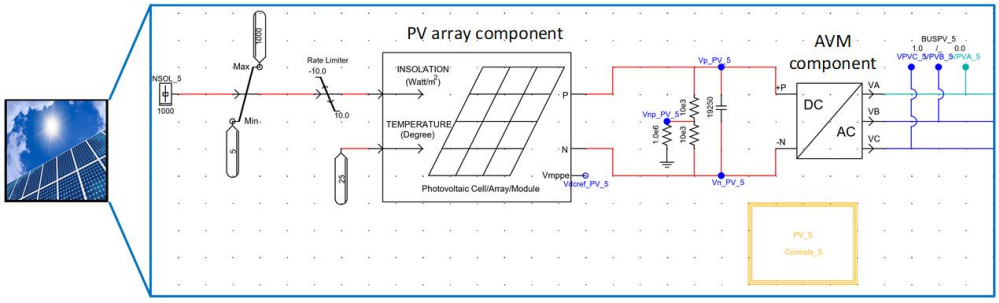

Figure 4.6. Components for solar PV system used in the variation model.

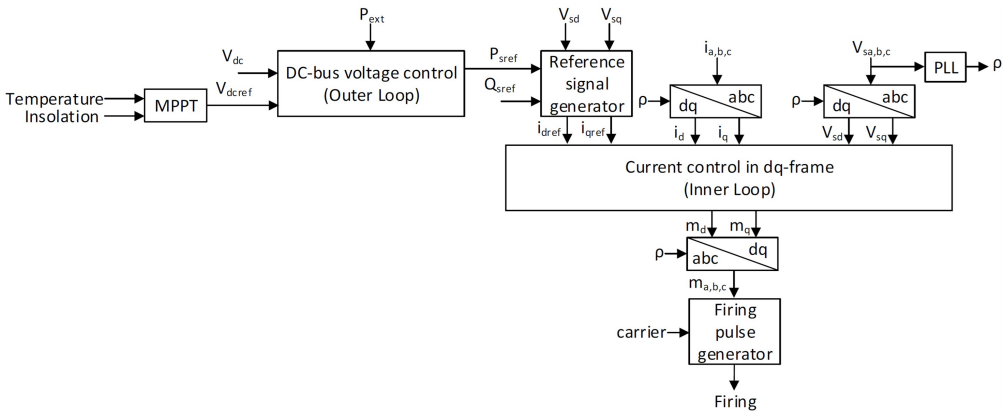

Figure 4.7. Block diagram of the inverter controls used for the PV system.

compared with those from the PSCAD [71] software. The modeling and parameters of the testbed are replicated identically in PSCAD software to confirm the operation of the representative model in RSCAD.

The performance of the transmission-distribution model is tested by comparing RTDS simulation results with those from PSCAD/EMTDC in terms of steady-state simulation testing and dynamic simulation testing. The steady-state simulation testing is focused on power flow solutions while the transient simulation testing was centered on the dynamics of voltage and current in the model under different faulted scenarios. The consistent results between RTDS simulation and PSCAD/EMTDC confirm the correct function of the constructed model. To avoid repetition, the comparison results for all the buses are not shown here.

4.3.1. Steady State Simulation Test

In this test, the power flow of each representative power system model under normal operating conditions has been evaluated by the RSCAD and PSCAD software, respectively. The following criterion has been used for verifying the models in the steady-state simulation testing:

Verification criterion for steady-state simulation testing: If RSCAD and PSCAD provide close power flow results in a representative power system model, the model has the correct operation under operating conditions under normal conditions.

The power flow results from the RSCAD and PSCAD software and the differences in the results between the two simulation platforms for the transmission side of the testbed is listed in Table 4.2. The difference in the power flow results for the distribution side of the model is listed in Table 4.3. It can be observed from Table 4.2 and Table 4.3 that the power flow results from

Table 4.2. Comparison of power flow results from RSCAD and PSCAD in the transmission side of the testbed.

Bus	RSCAD		PSCAD		Difference	
	Magnitude (p.u.)	Angle	Magnitude (p.u)	Angle	Magnitude (p.u.)	Angle
1	1.04	0°	1.04	0.101°	0	0.101°
2	1.025	9.65°	1.025	9.47°	0	0.18°
3	1.025	5.36°	1.025	5.24°	0	0.12°
4	1.025	-2.11°	1.024	-2.09°	0.001	0.02°
5	0.9953	-4.23°	0.9942	-3.82°	0.0011	0.41°
6	1.011	-3.99°	1.009	-3.56°	0.002	0.43°
7	1.025	4.45°	1.025	3.91°	0	0.54°
8	1.015	0.56°	1.014	0.94°	0.001	0.38°
9	1.031	2.16°	1.031	2.35°	0	0.19°

RSCAD were consistent with those from the PSCAD simulation. The maximum difference in voltage magnitude obtained is less than 0.04 p.u. and maximum voltage angle is less than 0.79°. The developed testbed adheres to the verification criteria for steady-state simulation testing and confirms accurate operation under the operating conditions without faults.

4.3.2. Dynamic Simulation Test

The dynamic simulation testing is to verify the functionality of the representative power system model under faulted operating conditions. Since the number of possible faulted condition conditions of an electrical grid operation is vast, representative faulted cases were selected to test the performance of the representative power system model given the limited number of possible tests. For the same fault event, the instantaneous and per-unit voltage and current waveforms at each fault bus have been simulated by RSCAD and PSCAD, respectively. The following criterion has been used for the verification of the model in this dynamic simulation testing:

Verification criterion for dynamic simulation testing: If RSCAD and PSCAD provide consistent faulted voltage and current waveforms in a representative power system model under each applied fault, the model has the correct operation under faulted operating conditions.

Few simulation results after testing the model in symmetrical and unsymmetrical faults at several locations are presented in the paper. Each fault was applied for 3 cycles in each location. The results show that the overall performances from RSCAD simulations were consistent with those

Table 4.3. Difference in power flow results from RSCAD and PSCAD in the distribution side of the testbed.

Bus	Magnitude (p.u.)			Angle		
	Phase A	Phase B	Phase C	Phase A	Phase B	Phase C
611			0.0139			0.07°
632	0.003	0.013	0.008	0.773°	0.33°	0.38°
633	0.006	0.01	0.013	0.453°	0.05°	0.01°
634	0.035	0.017	0.038	0.79°	0.49°	0.45°
645		0.013	0.007		0.51°	0.34°
646		0.014	0.01		0.25°	0.42°
650	0.0209	0.008	0.0169	0.07°	0.68°	0.19°
652	0.013			0.27°		
671	0.01	0.015	0.0168	0.04°	0.26°	0.32°
	0.014	0.013	0.0203	0.12°	0.18°	0.15°
680	0.014	0.012	0.0206	0.089°	0.46°	0.37°
684	0.013		0.0149	0.71°		0.12°
692	0.013	0.013	0.0158	0.26°	0.39°	0.1°
RG60	0.02	0.02	0.013	0.61°	0.1°	0.06°

from PSCAD simulations under different fault scenarios. The simulation results for a three-phase fault at the transmission side and a line-line-to-ground fault at the distribution side of the testbed are presented as an illustration.

4.3.2.1. Transmission Side Fault

Fig. 4.8 and Fig. 4.9 shows the instantaneous and per-unit voltage and current after a three-phase fault at bus 8 of the transmission side of the base model. The peak values of the instantaneous and per-unit currents from RSCAD simulation are about 3.2 kA and 5.4 p.u., respectively while those from PSCAD are about 4.2 kA and 7.2 p.u. Similarly, the peak values of the instantaneous and per-unit voltages from RSCAD and PSCAD simulations are different, especially at the clearing instant of fault. The differences mainly result from the different modeling approaches are adopted in RSCAD and PSCAD.

Also, it is noticed that the individual phases of instantaneous voltage or current have different dynamics in RSCAD and PSCAD simulations. For example, at the instant of fault, phase a voltage from RSCAD simulation is going to the negative half cycle while the one from PSCAD simulation is going to the positive half cycle. The similar differences in the dynamics of individual phase voltage

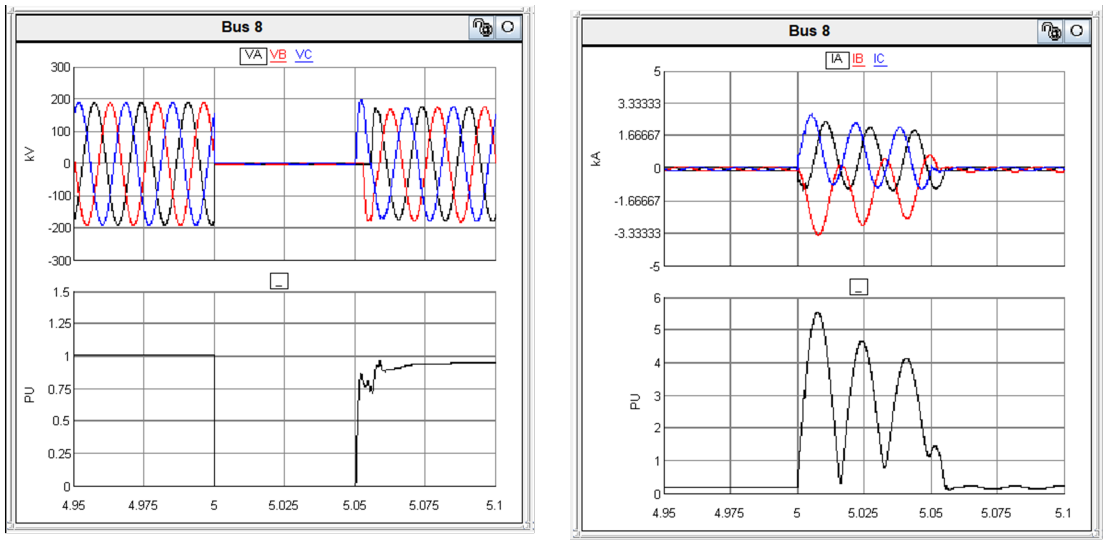

Figure 4.8. Instantaneous and per-unit voltage and current from RSCAD after a three-phase fault is applied at bus 8 of the transmission side of the testbed.

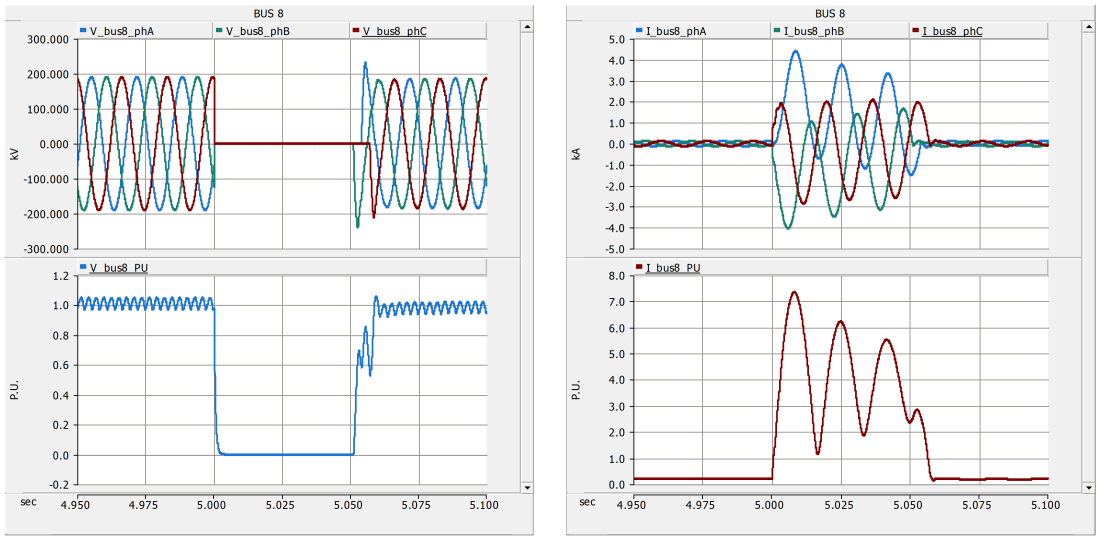

Figure 4.9. Instantaneous and per-unit voltage and current from PSCAD after a three-phase fault is applied at bus 8 of the transmission side of the testbed.

dynamics at the instant of fault and the clearing instant of fault can be observed as well. The differences are mainly from the different techniques are used in RSCAD and PSCAD to initialize operating conditions before the fault applied. However, the overall dynamic performances of voltage and current between the two simulation platforms matched well to each other. Based on the

verification criterion for dynamic simulation testing, the representative power system model thus has the correct operation under faulted operating conditions.

4.3.2.2. Distribution Side Fault

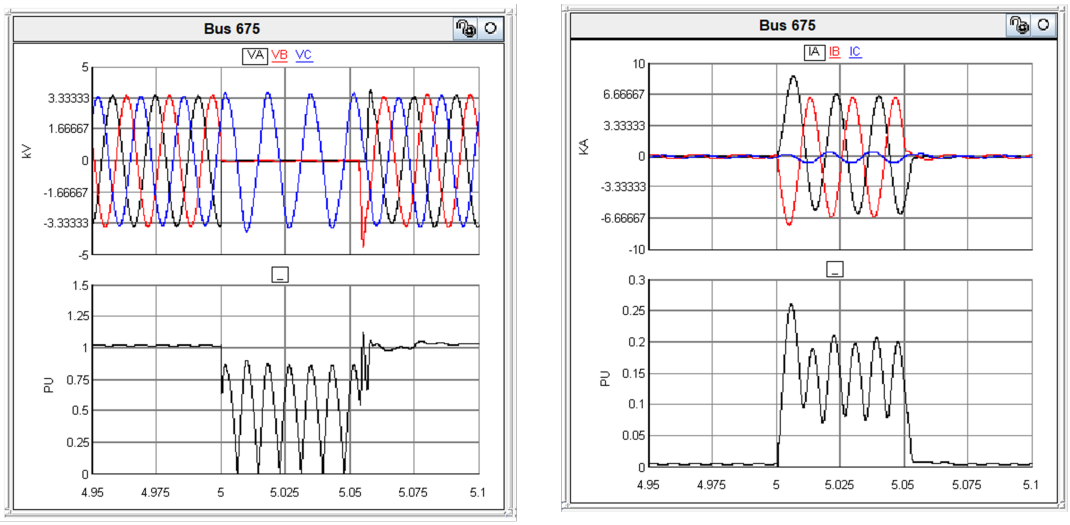

Figure 4.10. Instantaneous and per-unit voltage and current from RSCAD after a line-line-to-ground fault is applied at bus 675 of the distribution side of the testbed.

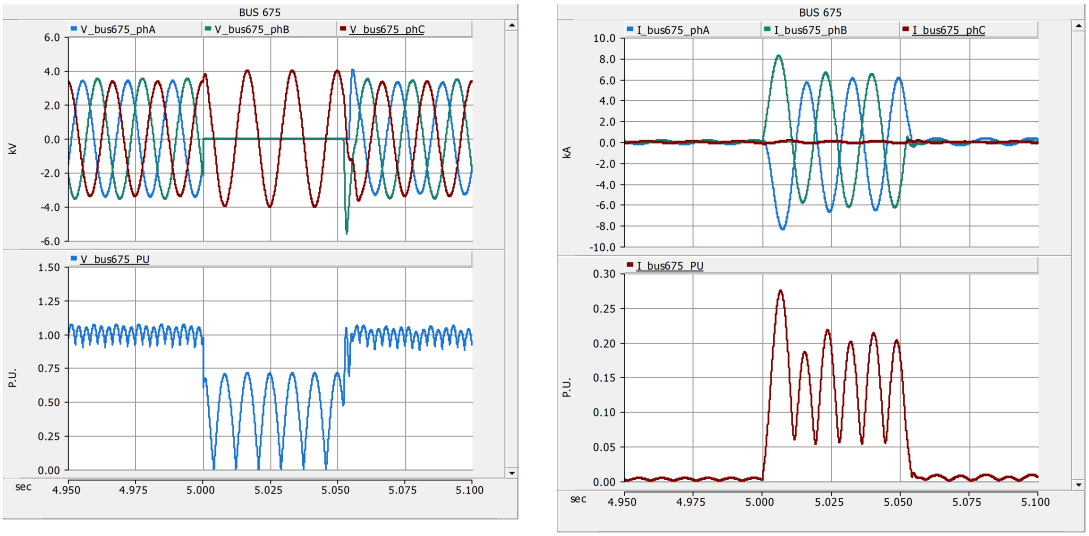

Figure 4.11. Instantaneous and per-unit voltage and current from PSCAD after a line-line-to-ground fault is applied at bus 675 of the distribution side of the testbed.

Similar to the dynamic simulation results tested in the transmission side, some simulation results in the variation model also have the different peak values of instantaneous and per-unit voltages (and currents) during the fault duration between the two simulation platforms. These differences can be seen from the simulation results for a line-line-to-ground fault at the distribution side of the model as shown in Fig. 4.10 and Fig. 4.11. In addition to these differences, the overall dynamic performances of voltage and current between the two simulation platforms matched well to each other for various faults applied in numerous locations. Based on the verification criterion for dynamic simulation testing, the distribution side dynamics demonstrated validated operation under faulted conditions.

4.4. Case Studies

With the transmission–distribution model constructed in Section 3, the impact of transmission-level disturbances on the operation of distributed solar PVs is investigated using the real-time electromagnetic transient simulation testbed based on RTDS. In the following transient simulation analysis, the simulation is performed based on the Dommel algorithm. The simulation time step is 100 µs, and the simulation time is 0.2 s. The transmission–distribution model has 114 nodes. In the model, five cases below are considered.

4.4.1. Impact of Fault Types in Transmission System on Solar PV Operation

In this case, different fault types in the transmission system are generated to investigate their impacts on the operation of solar PVs in the distribution system. The fault is applied at bus 6 in the transmission system. Four types of faults are considered, including a three-phase fault, a single line-to-ground fault, a line-to-line fault, and a double line-to-ground fault. Each type of fault has the same occurring and clearing times when it is applied at bus 6. Following different types of faults, the voltage and current of each solar PV bus in the distribution system are observed to analyze the responses of the five solar PVs in the distribution system. Fig. 4.12- 4.15 demonstrate the voltage and current responses at solar PV buses 634 and 680 under the four types of faults at bus 6 in the transmission system.

It can be observed from Fig. 4.12- 4.15 that the three-phase fault has a more severe impact on the solar PV operation than the other three types of unsymmetrical faults; among those three types of unsymmetrical faults, the double line-to-ground fault has the most severe impact. As shown in Fig. 4.12, the maximum transient voltage and current at solar PV bus 634 (or bus 680)

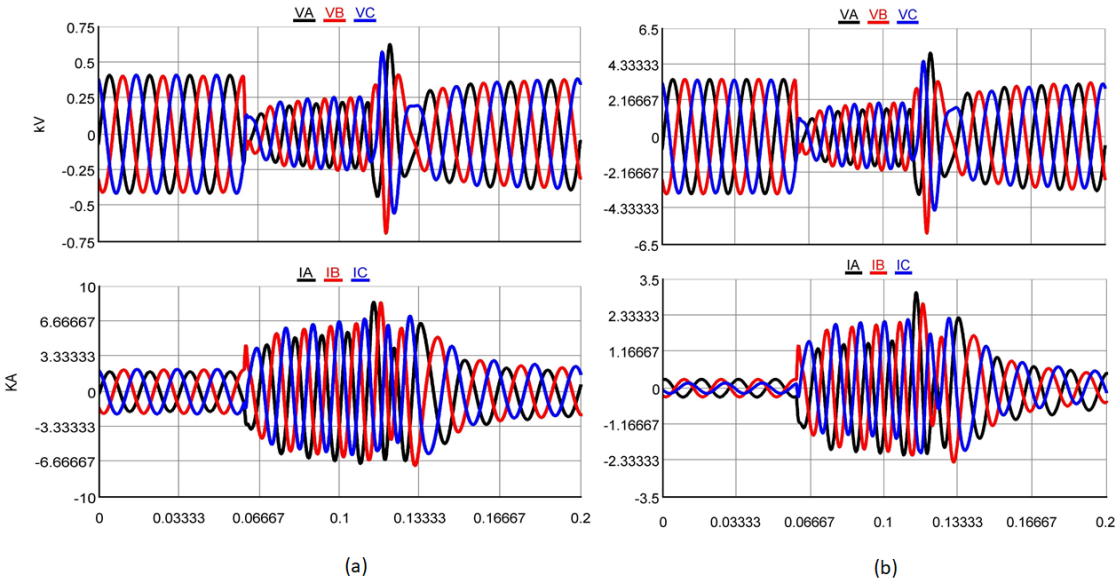

Figure 4.12. Three-phase fault applied at bus 6 in the transmission system of the testbed: (a) instantaneous voltage and current at bus 634; (b) instantaneous voltage and current at bus 680.

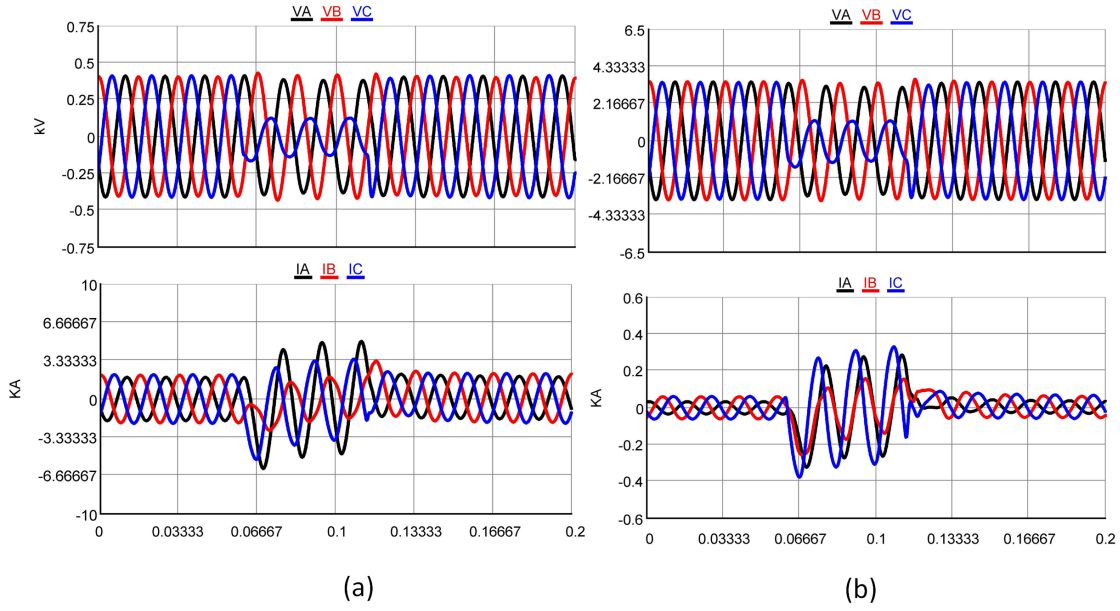

Figure 4.13. Single line-to-ground fault applied at bus 6 in the transmission system of the testbed: (a) instantaneous voltage and current at bus 634; (b) instantaneous voltage and current at bus 680.

following the three-phase fault are approximately 1.72 p.u. and 3.0 p.u. (1.75 p.u. and 17 p.u.), respectively, which are greater than those at bus 634 (or bus 680) following the other three types of unsymmetrical faults. Under a single line-to-ground fault, the maximum transient voltage at solar PV bus 634 (or bus 680) is smaller than 1.1 p.u., while the maximum transient current at solar PV

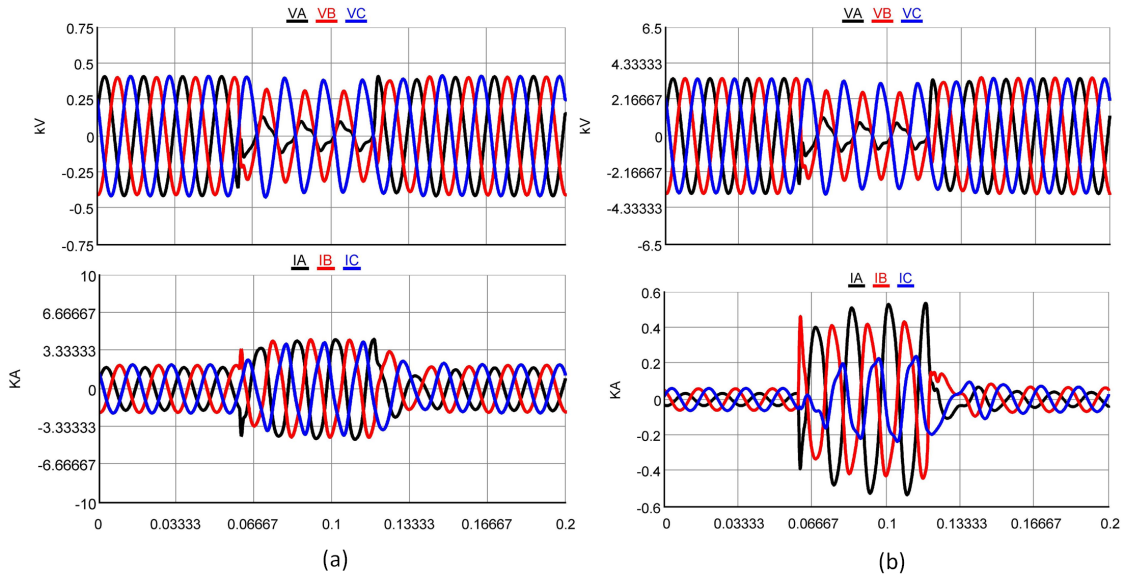

Figure 4.14. Line-to-line fault applied at bus 6 in the transmission system of the testbed: (a) instantaneous voltage and current at bus 634; (b) instantaneous voltage and current at bus 680.

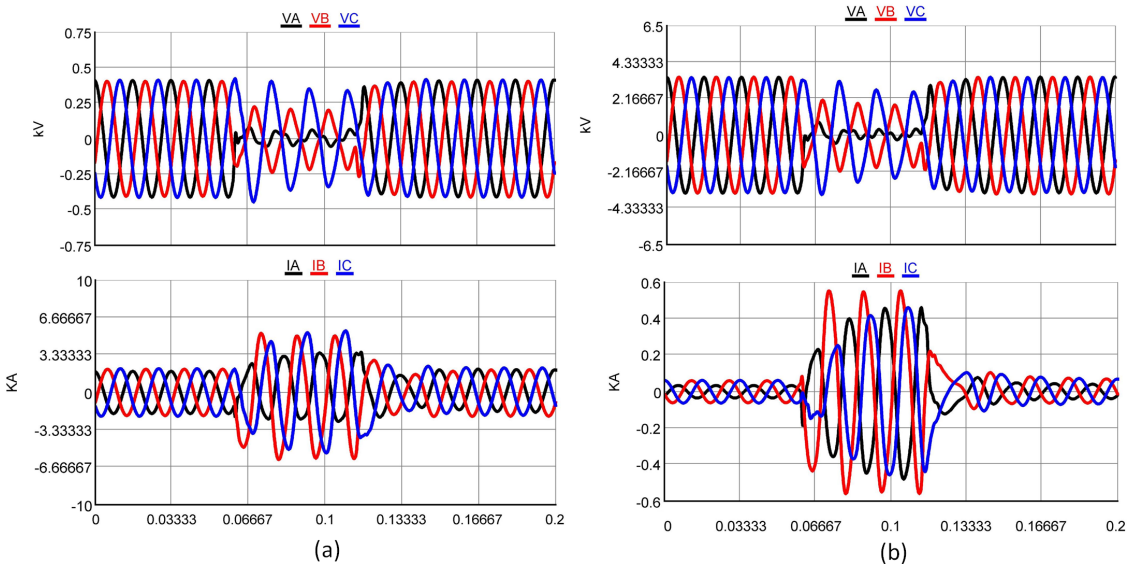

Figure 4.15. Double line-to-ground fault applied at bus 6 in the transmission system of the testbed: (a) instantaneous voltage and current at bus 634; (b) instantaneous voltage and current at bus 680.

bus 634 (or bus 680) is about 2.4 p.u. (6.8 p.u.). Under a line-to-line fault, the maximum transient voltage at solar PV bus 634 (or bus 680) is smaller than 1.0 p.u., and the maximum transient current at solar PV bus 634 (or bus 680) is about 2.0 p.u. (9.1 p.u.). Under a double line-to-ground fault, the maximum transient voltage at solar PV bus 634 (or bus 680) is still smaller than 1.0 p.u., and the maximum transient current at solar PV bus 634 (or bus 680) is about 2.0 p.u. (10.5 p.u.). The

transient voltage of different phases at solar PV bus 634 (or bus 680) for these unsymmetrical faults is lower than the normal operating voltage. Compared to the single line-to-ground fault and the line-to-line fault, the double line-to-ground fault on these solar PV buses is more severe.

4.4.2. Impact of Fault Locations in Transmission System on Solar PV Operation

In this case, the impact of fault locations in the transmission system on the operation of solar PVs in the distribution system is investigated. To this end, another fault with the same fault occurring and clearing time of the fault transpired at bus 6 is applied at bus 7 in the transmission system. Still, four types of faults at bus 7, including a three-phase fault, a single line-to-ground fault, a line-to-line fault, and a double line-to-ground fault, are considered. Following different types of faults at bus 7, the voltage and current of each solar PV bus are observed to analyze the responses of the five solar PVs in the distribution system. According to the previous analysis, it is known that when the fault is applied at bus 6, the three-phase fault has the most severe impact on the solar PV operation. For comparison, Fig. 4.16 shows the voltage and current responses at solar PV buses 634 and 680 under the three-phase fault at bus 7 in the transmission system.

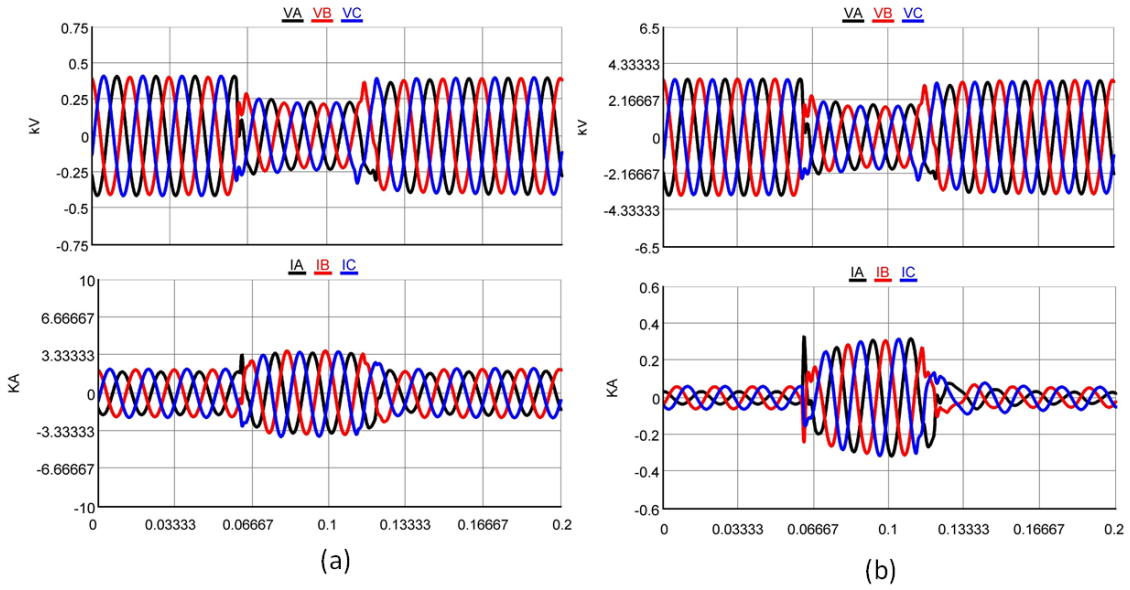

Figure 4.16. Three-phase fault applied at bus 7 in the transmission system of the testbed: (a) instantaneous voltage and current at bus 634; (b) instantaneous voltage and current at bus 680.

By comparing Fig. 4.16 with Fig. 4.12, it can be seen that when the fault location is moved far from the distributed solar PVs from bus 6 to bus 7 in the transmission system, the same fault

has a less severe impact on solar PV operation. Since bus 7 is further than bus 6 in the transmission system for all solar PVs in the distribution system, the maximum transient voltage and current at bus 634 (or bus 680) following the three-phase fault at bus 7 is smaller than those at bus 634 (or bus 680) following the three-phase fault at bus 6. For example, the maximum transient voltage and current at bus 680 resulting from the fault at bus 7 is less than 1.0 p.u. and 5.67 p.u., respectively, but those resulting from the fault at bus 6 are 1.75 p.u. and 17 p.u. Thus, when the transmission-level fault location is closer to the solar PV buses, it has a substantial influence on solar PV operation in the distribution system.

4.4.3. Impact of Solar Penetration Levels in Transmission System on Solar PV Operation

Under the identified severe transmission-level fault type and location, the impact of solar penetration level on solar PV operation is further investigated. More specifically, the penetration level of the integrated solar PVs is changed by decreasing the irradiance level from 1000 W/m^2 to 750 W/m^2. Then, under the three-phase fault at bus 6 in the transmission system, Fig. 4.17 shows the resulting voltage and current responses at solar PV bus 634 and bus 680 when solar PVs have the irradiance levels of 750 W/m^2.

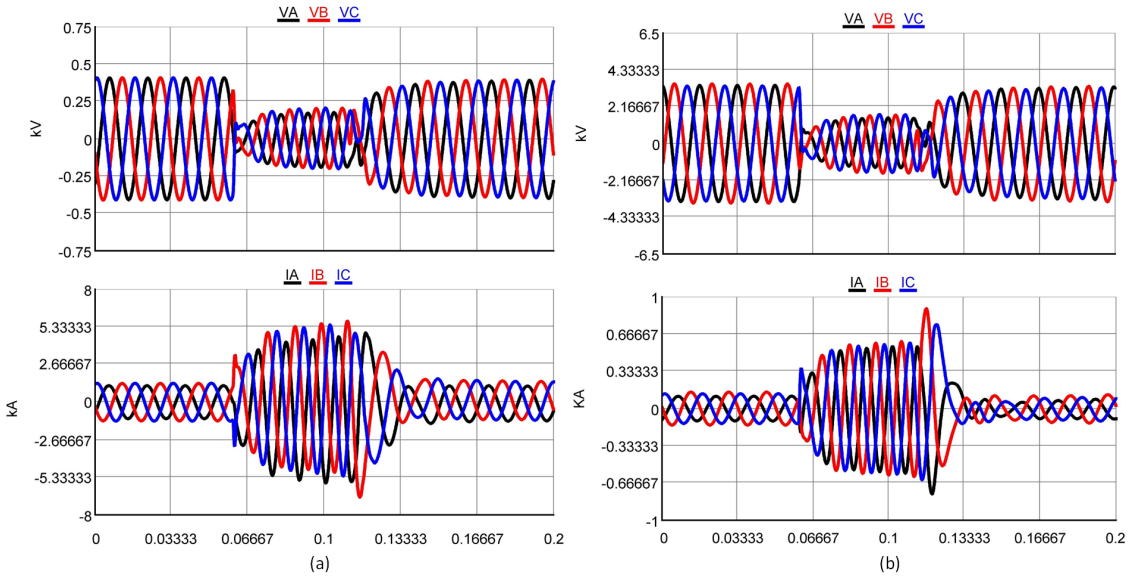

Figure 4.17. Three-phase fault applied at bus 6 in the transmission system of the testbed: (a) instantaneous voltage and current at bus 634 with 750 W/m^2 solar irradiance; (b) instantaneous voltage and current at bus 680 with 750 W/m^2.

By comparing Fig. 4.17 with Fig. 4.12, it can be seen that the severity of the impact of transmission-level disturbance on solar PV operation decreases with solar penetration level. As shown in Fig. 4.17, both the maximum transient voltage and current decrease with the solar penetration level due to the irradiance decrease to 750 W/m^2 from 1000 W/m^2. For example, the maximum transient current is around 14.0 p.u. at solar PV bus 680 following the three-phase fault at bus 6 in the transmission system when all solar PVs in the distribution system have 750 W/m^2 solar irradiance, while the maximum current is increased to 17.0 p.u. at solar PV bus 680 resulting from the same fault when all solar PVs have 1000 W/m^2 solar irradiance. The maximum transient voltage in the case with 750 W/m^2 solar irradiance does not exceed the normal range but with 1000 W/m^2 solar irradiance has a peak of 1.75 p.u. for bus 680.

4.4.4. Impact of Loading Levels in Transmission System on Solar PV Operation

Additionally, the impact of loading level on solar PV operation is investigated under the identified severe transmission-level fault type and location. In this case, the loading level is increased by four times its original loading level in the distribution system. Under the three-phase fault at bus 6 in the transmission system, the transient voltages and currents at the solar PV buses are investigated. For comparison, Fig. 4.18 shows the resulting voltage and current responses at solar PV bus 634 and bus 680 after the loading is increased.

By comparing Figures 4.12 and 4.18, it can be seen that the maximum transient voltage and current at bus 634 and bus 680 following the transmission-level fault at bus 6 are decreased with the increased loading. For example, before the loading level is increased in the distribution system following the transmission-level fault at bus 6, the maximum transient currents at solar PV bus 634 and bus 680 are approximately 3.0 p.u. and 17 p.u., respectively; after the loading is increased in the distribution system following the same transmission-level fault, the resulting maximum transient voltage and current decreases to 2.8 p.u. and 16.2 p.u. at bus 634 and bus 680.

4.4.5. Impact of Grid Strength on Solar PV Operation

To understand the relationship between the previous investigation results with grid strength, the impact of grid strength on the solar operation is further analyzed in the system. To assess grid strength, the site dependent short circuit ratio (SDSCR) [35] is used, which considers the interaction among solar PVs interconnected through the power network. The SDSCR at any point

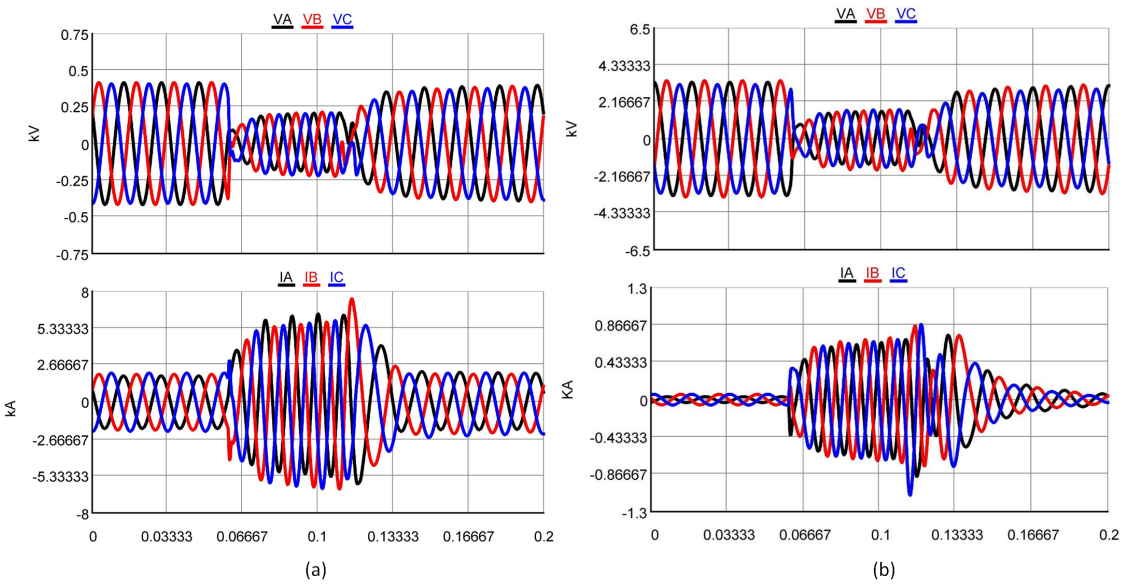

Figure 4.18. Three-phase fault applied at bus 6 in the transmission system of the testbed: (a) instantaneous voltage and current at bus 634 with increased loading; (b) instantaneous voltage and current at bus 680 with increased loading.

of interconnection (POI) i is calculated using the following Equation (4.1):

$$SDSCR_i = \frac{|V_{R,i}|^2}{(|P_{R,i} + \sum_{j \epsilon R, j \neq i} w_{ij} P_{R,j}|)|Z_{RR,ii}|} \tag{4.1}$$

$$w_{ij} = \frac{Z_{RR,ij}}{Z_{RR,ii}} . \left(\frac{V_{R,i}}{V_{R,j}}\right)^* \tag{4.2}$$

where R is the set of all POIs connected to IB-RERs; $Z_{RR,ij}$ is the (i^{th}, j^{th}) element in sub-matrix of bus impedance matrix that is only related to buses connected to IB-RERs; $V_{R,i}$ is the voltage at POI i; $P_{R,i}$ is the rated capacity or injected power from the IB-RER at POI i.

Based on the SDSCR defined in Equation (4.1), the grid strength at each POI of the solar PV in the distribution system in Fig 4.2 is evaluated. Table 4.4 lists the SDSCR values for the five POIs. If the SDSCR value is greater than 3, the grid is strong at the POI; if the SDSCR value is between 2 and 3, the grid is weak at the POI; if the SDSCR value is less than 2, the grid is very weak at the POI. Thus, it can be observed from Table 2 that buses 632, 634, and 675 are strong POIs since they have SDSCR values higher than 3. Bus 671 and 680 are the weak POIs as they have SDSCR values less than 3 but greater than 2.

Table 4.4. SDSCR values for solar PV buses in the distribution system.

Solar PV Buses	SDSCR Values
632	3.6346
634	3.3830
671	2.7768
675	3.0545
680	2.4765

4.5. Discussion

When comparing the evaluation results presented in Table 2 with the simulation results in Fig. 4.12- 4.18, the following conclusions can be obtained:

- By comparing Table 4.4 with Fig. 4.12- 4.15, it is found that undesirable transient dynamics may be more likely to occur at weaker POIs under the same fault but different types. Moreover, the severity of the undesirable transient dynamics at the weaker POIs may increase with the fault type. Table 4.4 shows that bus 680 is weaker than bus 634. Comparing the maximum transient voltage and current at bus 634 with those at bus 680, it can be observed from Figures 8-11 that the maximum transient voltage and current at bus 634 are smaller than those at bus 680 following the same transmission-level fault with the four different types. For example, when the single line-to-ground fault occurred in the transmission system, Fig. 4.13 shows that the maximum transient current at bus 634 is approximately 2.4 p.u., but the maximum transient current at bus 680 is approximately 6.8 p.u. Moreover, when the fault type is changed into the severest three-phase fault, Fig. 4.12 shows that the maximum transient voltage and current at bus 634 are approximately 1.72 p.u. and 3 p.u.; however, the maximum transient voltage and current at bus 680 are approximately 1.75 p.u. and 17 p.u.

- By comparing Table 4.4 with Fig. 4.16, it is also found that under the same three-phase fault but different locations, weak POIs are more likely to have undesirable transient dynamics. As shown in Table 4.4, bus 680 is weaker than bus 634. By comparing the maximum transient voltage and current at bus 634 with those at bus 680 in Fig. 4.12 and 4.16, it can be observed that when the three-phase fault is moved from bus 6 to bus 7 in the transmission system, the maximum current transient at bus 634 is decreased from 3 p.u. to 1.4 p.u.; the maximum

current transient at bus 680 is decreased from 17 p.u. to 5.67 p.u. Additionally, even when the fault is far from the distribution system (at bus 7), weak bus 680 is still more likely to have an undesirable transient response than bus 634.

- By comparing Table 4.4 with Figure 4.17, it is found that undesirable transient dynamics may be more likely to happen at weaker POIs under the increasing solar penetration level in the distribution system. Compared to bus 634, weak bus 680 has a more severe impact on solar PV operation following the same transmission-level fault. As shown in Fig. 4.17, for bus 680, when the solar irradiance is 750 W/m^2, the maximum transient current is 14 p.u.; as shown in Fig. 4.12, when solar irradiance is increased to 1000 W/m^2, the maximum transient current is 17 p.u. For bus 634, the maximum transient current is increased from about 2.2 p.u. to 3 p.u. when solar irradiance is increased from 750 W/m^2 to 1000 W/m^2.

- By comparing Table 4.4 with Fig. 4.18, it is found that increasing the loading level in the distribution system may decrease the risk of undesirable transient dynamics at weaker POIs following the transmission-level disturbance. As shown in Fig. 4.12 and 4.18, the severity of the impact of transmission-level disturbance on solar PV operation decreases with the increase in loading level in the distribution system. At the weak bus 680, this impact becomes relatively significant. Before increasing the loading level, the maximum transient current is 17 p.u. following the transmission-level fault at bus 6; the transient current is reduced to 16.2 p.u. following the same transmission-level fault when the loading level is increased. This change can improve grid strength at bus 680 and thus reduce the risk of undesirable transient dynamics of solar PV at bus 680.

4.6. Summary

In this dissertation, a real-time RTDS-based simulation testbed was presented to explore the impacts of realistic transmission-level disturbances on solar PV operation in the distribution system. The testbed includes detailed modeling of components in the transmission and distribution systems along with the detailed PV models and its inverter controls to capture the accurate dynamic behaviors of solar PVs in response to the transmission-level disturbances. The testbed was used to investigate the transient responses from the solar PV inverters under different transmission-level disturbances regarding different fault types and locations, solar penetration levels, and loading

levels. It is found that the grid strength at the POIs of solar PV inverters significantly affects the transient response from the solar PV inverters following the transmission-level disturbances. At weaker POIs, the transient response is more sensitive to the disturbances. Such sensitivity becomes more significant when the transmission-level disturbance is closer to the weak POIs or the disturbances become more severe. Additionally, the impact of the transmission-level disturbances on the solar PVs at the weak POIs exacerbate with the increasing solar penetration levels and loading levels. Thus, when an increasing number of IB-RERs are being integrated into the grid, it is important to study and develop new technologies for grid planning, operation, and protection in weak grid conditions to address the emerging issues of integrating the high penetration of solar PVs and other IB-RERs.

5. CONCLUSION AND FUTURE WORK

This dissertation investigated the impact of IB-RERs on grid operation at the transmission- and distribution- levels while considering uncertain operating conditions. The major conclusions are summarized as follows:

The PCM was used to quantify the impact of uncertainty in distribution sytem on grid operation. In the distrubtion system, uncertainty in IB-RER like wind speed, loading and solar irradiance were introduced to the PCM by probablistic distributions such as Weibull, Normal and Beta distributions. By the comparision with Monte Carlo simulations, it was shown that the PCM was able to achieve accurate mean and ballpark variance of the output variables and has a significantly smaller number of model runs than Monte Carlo before leveraging time and cost for detailed computational analysis.

With the PCM, a method was further developed to evaluate uncertainty in the transmisison sysetm for grid strength analysis. In the method, the SDSCR-based method and ESDSCR-based approach were used for grid strength assessment, while the PCM was used to establish the approximation polynomial functions with multiple input variables for modeling the impact of uncertain renewable generation. To improve the accuracy of the PCM approximation model, K-means clustering algorithm was incorporated into the PCM for selecting the most representative collocation points. The proposed melthod was tested on the modified IEEE 39-bus system with high penetration of solar PVs. The results show that the proposed method is promising for grid strength assessment while considering the impact of variable renewable generation to guide grid planning and operation for identifying potential weak grid issues.

In addtion, the impacts of transmission-level disturbances on solar PV operation in the distribution system were investigated using a real-time electromagnetic simulator, which can capture the accurate dynamic behaviors of solar PVs in response to the transmission-level disturbances via detailed modeling of components in the transmission and distribution systems along with the detailed PV models and its inverter controls. It is found that the grid strength at the POIs of solar PV inverters signicantly affects the transient response from the solar PV inverters following the transmission-level disturbances. The impact of the transmission-level disturbances on the solar PVs

at the weak POIs exacerbate with the increasing solar penetration levels and loading levels. Thus, when an increasing number of IB-RERs are being integrated into the grid,it is important to study and develop new technologies for grid planning, operation, and protection in weak grid conditions to address the emerging issues of integrating the high penetration of solar PVs and other IB-RERs.

The dependencies among the uncertainties will be an important factor to consider with regards to the renewable generation mix in the modern grid. For further extension of the research, the proposed algorithm can account for the correlation between IB-RERs by using numerous methods like Copula theory, Gaussian mixture model, etc. Also, the most important uncertainties in the power systems can be identified so that efficient modeling can be achieved to identify the weak grids. Further, the approximations from the algorithm can be tested with different contingencies in the network, to evaluate the efficacy for abnormal conditions.

REFERENCES

[1] U.S. Energy Information Administration,. (2021) "renewables became the second-most prevalent u.s. electricity source in 2020." Accessed: Dec 25, 2021. [Online]. Available: https://www.eia.gov/todayinenergy/detail.php?id=48896

[2] Statista,. (2021) "cumulative capacity of renewable energy in the u.s. from 2009 to 2020, by technology." Accessed: Dec 25, 2021. [Online]. Available: https://www.statista.com/statistics/499157/cumulative-capacity-of-renewables-in-the-us-by-technology/

[3] J. V. Milanović, "Probabilistic stability analysis: the way forward for stability analysis of sustainable power systems," *Philosophical Transactions of the Royal Society A: Mathematical, Physical and Engineering Sciences*, vol. 375, no. 2100, p. 20160296, 2017.

[4] M. D. Webster, M. A. Tatang, and G. J. McRae, "Application of the probabilistic collocation method for an uncertainty analysis of a simple ocean model," *MIT joint program on the science and policy of global change*, 1996.

[5] L. Fan, Z. Miao, and M. Zhang, "Subcycle overvoltage dynamics in solar pvs," *IEEE Transactions on Power Delivery*, vol. 36, no. 3, pp. 1847–1858, 2020.

[6] North America Electric Reliability Corporation (NERC), "1,200 MW fault induced solar photovoltaic resource interruption disturbance report," Atlanta,GA,USA, Tech. Rep., 2016.

[7] NERC, "900 MW fault induced solar photovoltaic resource interruption disturbance report," Atlanta,GA,USA, Tech. Rep., 2018.

[8] NERC, "Fault induced solar photovoltaic resource interruption disturbances report: Southern california events: April 20, 2018 and may 11, 2018," Atlanta,GA,USA, Tech. Rep., 2019.

[9] Joint NERC and Western Electricity Coordinating Council (WECC) Staff, "San fernando disturbance southern california event: 7 july 2020 joint nerc and wecc staff report," Atlanta, GA, USA, Tech. Rep., 2020.

[10] M. Maharjan, A. Banerjee, and R. G. Kavasseri, "Uncertainty analysis in distribution networks integrated with renewables by probabilistic collocation method," in *2020 52nd North American Power Symposium (NAPS)*. IEEE, 2021, pp. 1–6.

[11] M. Aien, A. Hajebrahimi, and M. Fotuhi-Firuzabad, "A comprehensive review on uncertainty modeling techniques in power system studies," *Renewable and Sustainable Energy Reviews*, vol. 57, pp. 1077–1089, 2016.

[12] J. R. Hockenberry and B. C. Lesieutre, "Evaluation of uncertainty in dynamic simulations of power system models: The probabilistic collocation method," *IEEE Transactions on Power Systems*, vol. 19, no. 3, pp. 1483–1491, 2004.

[13] R. Preece, N. C. Woolley, and J. V. Milanović, "The probabilistic collocation method for power-system damping and voltage collapse studies in the presence of uncertainties," *IEEE Transactions on Power Systems*, vol. 28, no. 3, pp. 2253–2262, 2012.

[14] L. Meiyan, M. Jin, and Z. Y. Dong, "Uncertainty analysis of load models in small signal stability," in *2009 International Conference on Sustainable Power Generation and Supply*, 2009, pp. 1–6.

[15] H. Dong, M. Jin, and H. Renmu, "Effect of uncertainties in parameters of load model on dynamic stability based on probabilistic collocation method," in *2007 IEEE Lausanne Power Tech*. IEEE, 2007, pp. 1100–1104.

[16] G. Pierrou and X. Wang, "The effect of the uncertainty of load and renewable generation on the dynamic voltage stability margin," in *2019 IEEE PES Innovative Smart Grid Technologies Europe (ISGT-Europe)*. IEEE, 2019, pp. 1–5.

[17] Y. Zhou, Y. Wan, S. Roy, C. Taylor, C. Wanke, D. Ramamurthy, and J. Xie, "Multivariate probabilistic collocation method for effective uncertainty evaluation with application to air traffic flow management," *IEEE Transactions on Systems, Man, and Cybernetics: Systems*, vol. 44, no. 10, pp. 1347–1363, 2014.

[18] C. Yan, L. Zhou, W. Yao, J. Wen, and S. Cheng, "Probabilistic small signal stability analysis of power system with wind power and photovoltaic power based on probability collocation method," *Global Energy Interconnection*, vol. 2, no. 1, pp. 19–28, 2019.

[19] K. N. Hasan, R. Preece, and J. V. Milanović, "Existing approaches and trends in uncertainty modelling and probabilistic stability analysis of power systems with renewable generation," *Renewable and Sustainable Energy Reviews*, vol. 101, pp. 168–180, 2019.

[20] A. Soroudi, M. Aien, and M. Ehsan, "A probabilistic modeling of photo voltaic modules and wind power generation impact on distribution networks," *IEEE Systems Journal*, vol. 6, no. 2, pp. 254–259, 2012.

[21] P. Davis and P. Rabinowitz, *Numerical Methods of Integration.* Academic Press, New York, 1975.

[22] C. Zheng and M. Kezunovic, "Impact of wind generation uncertainty on power system small disturbance voltage stability: A pcm-based approach," *Electric Power Systems Research*, vol. 84, no. 1, pp. 10–19, 2012.

[23] Keyou Wang, Guojie Li, and Xiuchen Jiang, "Applying probabilistic collocation method to power flow analysis in networks with wind farms," in *2013 IEEE Power Energy Society General Meeting*, 2013, pp. 1–5.

[24] Y. M. Atwa, E. F. El-Saadany, M. M. A. Salama, and R. Seethapathy, "Optimal renewable resources mix for distribution system energy loss minimization," *IEEE Transactions on Power Systems*, vol. 25, no. 1, pp. 360–370, 2010.

[25] K. Schneider, B. Mather, B. Pal, C.-W. Ten, G. Shirek, H. Zhu, J. Fuller, J. Pereira, L. Ochoa, L. De Araujo *et al.*, "Analytic considerations and design basis for the ieee distribution test feeders," *IEEE Transactions on power systems*, vol. 33, no. 3, pp. 3181–3188, 2017.

[26] J. LeSage, "Systems-level microgrid simulation from simple one-line diagram." [Online]. Available: https://www.mathworks.com/matlabcentral/fileexchange/67060-systems-level-microgrid-simulation-from-simple-one-line-diagram

[27] W. Gautschi, "Opq: A matlab suite of programs for generating orthogonal polynomials and related quadrature rules," *Disponibile presso http://www. cs. purdue. edu/archives/2002/wxg/codes/OPQ. html*, 2002.

[28] M. Maharjan, A. Ekic, and D. Wu, "Probabilistic grid strength assessment of power systems with uncertain renewable generation based on probabilistic collocation method„" in *17th International Conference on Probabilistic Methods Applied to Power Systems (PMAPS)*. IEEE, 2022 (submitted) .

[29] NERC. (2017) Integrating Inverter-Based Resources into Low Short Circuit Strength Systems. Reliability Guideline. Accessed on: December 18, 2020. [Online]. Available: https://www.nerc.com/comm/PC_Reliability_Guidelines_DL/Item_4a._Integrating%20_Inverter-Based_Resources_into_Low_Short_Circuit_Strength_Systems_-_2017-11-08-FINAL.pdf

[30] Y. Ding, P. Wang, L. Goel, P. C. Loh, and Q. Wu, "Long-term reserve expansion of power systems with high wind power penetration using universal generating function methods," *IEEE Transactions on Power Systems*, vol. 26, no. 2, pp. 766–774, 2010.

[31] Y. Ding, C. Singh, L. Goel, J. Østergaard, and P. Wang, "Short-term and medium-term reliability evaluation for power systems with high penetration of wind power," *IEEE Transactions on Sustainable Energy*, vol. 5, no. 3, pp. 896–906, 2014.

[32] NERC, "Nerc essential reliability services task force: measures framework report." 2015. [Online]. Available: http://www.nerc.com/comm/Other/essntlrlbltysrvcstskfrcDL/ERSTF%20Framework%20Report%20-%20Final.pdf.

[33] Y. Zhang, S.-H. F. Huang, J. Schmall, J. Conto, J. Billo, and E. Rehman, "Evaluating system strength for large-scale wind plant integration," in *2014 IEEE PES General Meeting Conference & Exposition*. IEEE, 2014, pp. 1–5.

[34] General Electric, *Minnesota Renewable Energy Integration and Transmission Study*. Minnesota Utilities & Transmission Companies and Minnesota Department of Commerce, 2014.

[35] D. Wu, G. Li, M. Javadi, A. M. Malyscheff, M. Hong, and J. N. Jiang, "Assessing impact of renewable energy integration on system strength using site-dependent short circuit ratio," *IEEE Transactions on Sustainable Energy*, vol. 9, no. 3, pp. 1072–1080, 2017.

[36] A. Ekic, B. Strombeck, D. Wu, and G. Ji, "Assessment of grid strength considering interactions between inverter-based resources and shunt capacitors," in *2020 IEEE Power & Energy Society General Meeting (PESGM)*. IEEE, 2020, pp. 1–5.

[37] R. Billiton and W. Li, *Reliability assessment of electric power systems using Monte Carlo methods*. New York: Spring, 1994.

[38] P. Krishayya, R. Adapa, M. Holm *et al.*, "Ieee guide for planning dc links terminating at ac locations having low short-circuit capacities, part i: Ac/dc system interaction phenomena," *CIGRE, France*, 1997.

[39] J. Zhang, C. Tse, K. Wang, and C. Chung, "Voltage stability analysis considering the uncertainties of dynamic load parameters," *IET generation, transmission & distribution*, vol. 3, no. 10, pp. 941–948, 2009.

[40] M. Fan, Z. Li, T. Ding, L. Huang, F. Dong, Z. Ren, and C. Liu, "Uncertainty evaluation algorithm in power system dynamic analysis with correlated renewable energy sources," *IEEE Transactions on Power Systems*, 2021.

[41] Australian Energy Market Operator, "System strength in the nem explained," 2020.

[42] Y. Zhu and D. Brown, "Prepare to meet the challenges in regional transmission planning and development," in *2015 IEEE Power & Energy Society General Meeting*. IEEE, 2015, pp. 1–5.

[43] I. S. C1204-1997, "Ieee guide for planning dc links terminating at ac locations having low short-circuit capacities," 1997.

[44] Y. Liu and Z. Chen, "A flexible power control method of vsc-hvdc link for the enhancement of effective short-circuit ratio in a hybrid multi-infeed hvdc system," *IEEE Transactions on Power Systems*, vol. 28, no. 2, pp. 1568–1581, 2012.

[45] W. Chenxu, T. Fei, Z. Hongsheng, Z. Yixi, L. Chang, and W. Feifei, "An improved cumulant method for probabilistic load flow calculation," in *2019 IEEE Power & Energy Society General Meeting (PESGM)*. IEEE, 2019, pp. 1–5.

[46] Manitoba Hydro International Ltd.,. (2021) "type 3 wind turbine generators (wtg)." Accessed: June 25, 2021. [Online]. Available: https://www.pscad.com/knowledge-base/article/496

[47] "NREL solar radiation research laboratory," Available: http://www.blowinglotsofweirdstuffup.com/guide.html (Accessed on:12/18/2021).

[48] S. Surender Reddy, P. R. Bijwe, and A. R. Abhyankar, "Real-time economic dispatch considering renewable power generation variability and uncertainty over scheduling period," *IEEE Systems Journal*, vol. 9, no. 4, pp. 1440–1451, 2015.

[49] J. D. Cook. (2017) Orthogonal polynomials and the beta distribution. Accessed on: December 18, 2020. [Online]. Available: https://www.johndcook.com/blog/2017/11/20/ortho-poly-beta/

[50] W. Gautschi, "Orthogonal polynomials (in matlab)," *Journal of computational and applied mathematics*, vol. 178, no. 1-2, pp. 215–234, 2005.

[51] P. J. Davis and P. Rabinowitz, *Methods of numerical integration*. Courier Corporation, 2007.

[52] W. Chen, X. Xie, D. Wang, H. Liu, and H. Liu, "Probabilistic stability analysis of subsynchronous resonance for series-compensated dfig-based wind farms," *IEEE Transactions on Sustainable Energy*, vol. 9, no. 1, pp. 400–409, 2017.

[53] "NREL solar radiation research laboratory," Available: http://www.blowinglotsofweirdstuffup.com/guide.html (Accessed on:12/18/2021).

[54] M. Maharjan, A. Ekic, B. Strombeck, and D. Wu, "An rtds-based testbed for investigating the impacts of transmission-level disturbances on solar pv operation," *Energies*, vol. 14, no. 13, p. 3867, 2021.

[55] S. Kang, H. Shin, G. Jang, and B. Lee, "Impact analysis of recovery ramp rate after momentary cessation in inverter-based distributed generators on power system transient stability," *IET Generation, Transmission & Distribution*, 2021.

[56] B. J. Pierre, M. E. Elkhatib, and A. Hoke, "Photovoltaic inverter momentary cessation: Recovery process is key," in *2019 IEEE 46th Photovoltaic Specialists Conference (PVSC)*. IEEE, 2019, pp. 1561–1565.

[57] N. Choi, B. Park, H. Cho, and B. Lee, "Impact of momentary cessation voltage level in inverter-based resources on increasing the short circuit current," *Sustainability*, vol. 11, no. 4, p. 1153, 2019.

[58] S. Zhu, D. Piper, D. Ramasubramanian, R. Quint, A. Isaacs, and R. Bauer, "Modeling inverter-based resources in stability studies," in *2018 IEEE Power & Energy Society General Meeting (PESGM)*. IEEE, 2018, pp. 1–5.

[59] H. Shin, J. Jung, and B. Lee, "Determining the capacity limit of inverter-based distributed generators in high-generation areas considering transient and frequency stability," *IEEE Access*, vol. 8, pp. 34 071–34 079, 2020.

[60] B. Mather and F. Ding, "Distribution-connected pv's response to voltage sags at transmission-scale," in *2016 IEEE 43rd Photovoltaic Specialists Conference (PVSC)*. IEEE, 2016, pp. 2030–2035.

[61] B. Mather, O. Aworo, R. Bravo, and P. D. Piper, "Laboratory testing of a utility-scale pv inverter's operational response to grid disturbances," in *2018 IEEE Power & Energy Society General Meeting (PESGM)*. IEEE, 2018, pp. 1–5.

[62] R. W. Kenyon, B. Mather, and B.-M. Hodge, "Coupled transmission and distribution simulations to assess distributed generation response to power system faults," *Electric Power Systems Research*, vol. 189, p. 106 746, 2020.

[63] H. Shin, J. Jung, S. Oh, K. Hur, K. Iba, and B. Lee, "Evaluating the influence of momentary cessation mode in inverter-based distributed generators on power system transient stability," *IEEE Transactions on Power Systems*, vol. 35, no. 2, pp. 1618–1626, 2019.

[64] C. Li and R. Reinmuller, "Fault responses of inverter-based renewable generation: on fault ride-through and momentary cessation," in *2018 IEEE Power & Energy Society General Meeting (PESGM)*. IEEE, 2018, pp. 1–5.

[65] B. J. Pierre, M. E. Elkhatib, and A. Hoke, "Pv inverter fault response including momentary cessation, frequency-watt, and virtual inertia," in *2018 IEEE 7th World Conference on Photovoltaic Energy Conversion (WCPEC)(A Joint Conference of 45th IEEE PVSC, 28th PVSEC & 34th EU PVSEC)*. IEEE, 2018, pp. 3660–3665.

[66] RTDS Teachnologies Inc,. (2021) Accessed: June 25, 2021. [Online]. Available: https://www.rtds.com

[67] P. W. Sauer, M. A. Pai, and J. H. Chow, *Power system dynamics and stability: with synchrophasor measurement and power system toolbox*. John Wiley & Sons, 2017.

[68] W. H. Kersting, *Distribution system modeling and analysis*. CRC press, 2006.

[69] IEEE PES AMPS DSAS Test Feeder Working Group. (2021) Accessed: June 25, 2021. [Online]. Available: https://site.ieee.org/pes-testfeeders/resources/

[70] J. J. Grainger and W. D. Stevenson, *Power system analysis*. McGraw-Hill, 2003.

[71] Manitoba Hydro International Ltd.,. (2021) Accessed: June 25, 2021. [Online]. Available: https://www.pscad.com/